CMS Physics Analysis Summary

Contact: cms-pag-conveners-susy@cern.ch 2016/03/24

Search for direct production of top squark pairs decaying to all-hadronic final states in pp collisions at $\sqrt{s} = 13$ TeV

The CMS Collaboration

Abstract

A search for top squarks in events with jets and missing transverse momentum is presented. The data were collected in proton-proton collisions at a center-of-mass energy of 13 TeV with the CMS detector at the LHC and correspond to an integrated luminosity of 2.3 fb^{-1}. Events are categorized by the properties of reconstructed jets, the presence of top quark candidates, and missing transverse momentum. No statistically significant excess of events above the expected contribution from standard model processes is observed. Exclusion limits are set in the context of simplified models of top squark pair production.

1 Introduction

Supersymmetry (SUSY) [1–5] is an extension to the standard model (SM) of particle physics that postulates a symmetry between fermions and bosons. For each SM particle a SUSY particle, or 'sparticle,' is proposed with the same quantum numbers except that its spin differs by a half-integer. In R-parity conserving models [6, 7], sparticles are produced in pairs and the lightest SUSY particle (LSP) is stable. Models with a weakly interacting neutralino ($\widetilde{\chi}_1^0$) as the LSP are particularly compelling because the $\widetilde{\chi}_1^0$ would be an excellent dark matter candidate [8]. The radiative corrections involving these sparticles protect the Higgs mass against divergent corrections, solving the gauge hierarchy or 'naturalness' problem [9–14]. However, sparticle masses cannot be arbitrarily large and the top squark ($\widetilde{\mathrm{t}}$) is expected to be one of the lightest sparticles in order to maintain 'natural' levels of fine tuning [15–19]. Based on these considerations, it is of particular interest to search for $\widetilde{\mathrm{t}}\bar{\widetilde{\mathrm{t}}}$ production with the decay of each sparticle ending in a $\widetilde{\chi}_1^0$ and SM particles. Run 1 SUSY searches at the CERN LHC [20] found no evidence of physics beyond the SM and these results place limits on the top squark mass, $m(\widetilde{\mathrm{t}})$, extending to 775 GeV in some scenarios [21–26].

This document describes such a search in the all-hadronic final state. This final state has the largest accessible production rate for the signal models studied, corresponding to the ∼45% of signal events in which the W bosons produced in the top squark decay chains decay to quark pairs. We consider two top squark decay scenarios within the Simplified Model Spectra (SMS) framework [27–29]. In the scenario denoted as 'T2tt', the $\widetilde{\mathrm{t}}$ has a single decay mode, via a top quark: $\widetilde{\mathrm{t}} \to \mathrm{t}\widetilde{\chi}_1^0$, in which the $\widetilde{\chi}_1^0$ is the LSP. A second, mixed decay scenario, denoted 'T2tb' involves two $\widetilde{\mathrm{t}}$ decay modes, via a top quark or via the lightest chargino ($\widetilde{\mathrm{t}} \to \mathrm{b}\widetilde{\chi}_1^{\pm}$) with the chargino subsequently decaying to a virtual W boson and a $\widetilde{\chi}_1^0$. A 50% branching ratio for each decay mode is assumed for the T2tb models studied. Figure 1 shows the diagrams representing these two simplified models. Each of these scenarios share the same final-state particles: $\mathrm{b\bar{b}qqqq}\widetilde{\chi}_1^0$. The neutralinos and charginos present in these cascades are states that are formed via linear combinations of the superpartners of the SM gauge bosons and the SUSY Higgs bosons, the gauginos and higgsinos respectively. A natural simplified SUSY spectrum is assumed in which the $\widetilde{\chi}_1^{\pm}$ are 5 GeV heavier than the $\widetilde{\chi}_1^0$. The $\widetilde{\chi}_1^0$ does not interact with the detector, resulting in missing transverse momentum ($\vec{p}_{\mathrm{T}}^{\,\mathrm{miss}}$). The magnitude of the missing transverse momentum, $\not{E}_{\mathrm{T}}$, is one of the most important discriminators between signal and SM background.

In this search we select events with no identified leptons, large $\not{E}_{\mathrm{T}}$, multiple jets and at least one jet identified as originating from the hadronization of a b quark. One of the dominant sources of the SM background originates from $\mathrm{t\bar{t}}$ or W boson production in association with jets in events with leptonic W boson decays. Events in which a Z boson, produced in association with jets, decays to neutrinos also provide a significant contribution to the SM background. Two independent analyses are performed, both of which are sensitive to a range of signal topologies. They rely on the use of top quark tagging algorithms and the categorization of events into exclusive search regions based on kinematic observables related to jets and $\not{E}_{\mathrm{T}}$. These two studies can be briefly described as:

- "High purity top tagging" (HPTT) analysis: An analysis that utilizes a high purity top tagging algorithm to identify top quarks. Events are categorized into exclusive search regions defined by the transverse mass (M_{T}) between b jets and $\not{E}_{\mathrm{T}}$, the number of reconstructed jets, the number of identified b jets, the presence or absence of a reconstructed top, and different $\not{E}_{\mathrm{T}}$ thresholds. The HPTT analysis is designed to have improved sensitivity for mixed decay (T2tb) models, and compressed T2tt

models with a small mass difference (Δm) between the $\widetilde{\mathrm{t}}$ and $\widetilde{\chi}_1^0$, including models in which the $\widetilde{\mathrm{t}}$ decays via an off-shell top quark.

- "High efficiency top tagging" (HETT) analysis: An analysis that relies on a custom, highly efficient algorithm to tag top-like objects in events and uses their kinematic properties as input to the computation of the "stransverse" mass (M_{T2}) variable [30, 31]. Exclusive search regions are constructed using the number of identified b jets and top-like objects, and different thresholds on $\not\!\!E_{\mathrm{T}}$ and M_{T2}. The HETT analysis is largely oriented towards T2tt models with medium to large Δm between the $\widetilde{\mathrm{t}}$ and $\widetilde{\chi}_1^0$.

Both analyses estimate the principal SM backgrounds with data control samples (CS) that are orthogonal but kinematically similar to the search sample. The selection criteria for these control samples are chosen to yield a sample with high purity for a particular background process. The control samples are also chosen to exhibit characteristics similar to those of the search sample, with significantly larger statistics whenever possible, in order to identify rare effects that can potentially affect the search regions. With the aid of simulated data samples, the experimental measurement of each background process in its corresponding data control sample is translated into a prediction for the number of SM events in each of the search regions. Although the approaches are similar, the two analyses complement each other since the predictions of the dominant background processes are based on different sets of assumptions and control regions.

The search is performed on a data sample corresponding to an integrated luminosity of 2.3 fb^{-1} of proton-proton collisions collected at a center-of-mass energy of 13 TeV with the CMS detector at the LHC. The event reconstruction and simulation are described in Section 2. Details of the event categorization and SM background estimation strategies for the two analyses are presented in Sections 3 and 4, along with the corresponding results. Interpretations in the context of the SMS framework are discussed in Section 5, followed by a summary in Section 6.

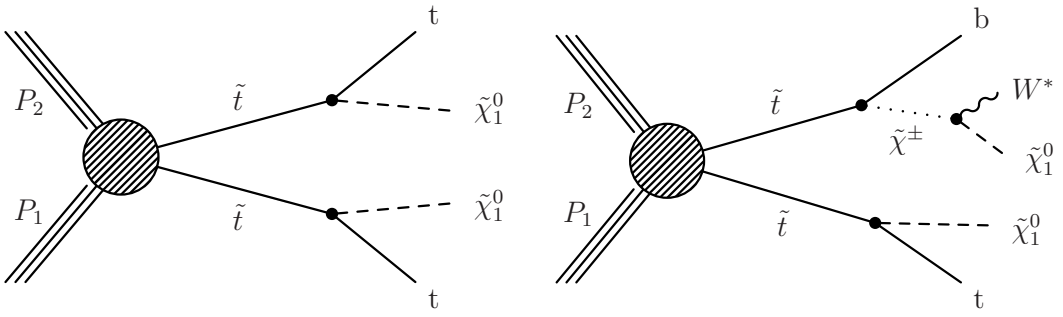

Figure 1: Diagrams representing the two simplified models of direct top squark pair production considered in this study: the T2tt model with top squark decay via a top quark (left), and the T2tb model with the top squark decaying either via a top quark or via an intermediate chargino (right).

2 Event reconstruction and simulation

2.1 Event reconstruction

The event reconstruction is performed using the particle-flow (PF) algorithm [32, 33], combining information from the tracker, calorimeter, and muon systems in order to identify charged hadrons, neutral hadrons, photons, muons, and electrons in an event. The $\vec{p}_{\mathrm{T}}^{\,\mathrm{miss}}$ is computed as the negative vector sum of the transverse momenta of all particle-flow candidates reconstructed

in an event. Events selected for the search are required to pass filters designed to remove detector- and beam-related noise and must have at least one reconstructed vertex. The reconstructed vertex with the largest $\sum p_T^2$ of associated tracks is designated as the event primary vertex. Charged particles originating from the primary vertex, photons, and neutral hadrons are clustered into jets using the anti-k_T algorithm [34] with a distance parameter of 0.4. The jet energy is corrected to account for the contribution of additional pileup interactions in an event and to compensate for variations in the detector response. Jets originating from b quarks are identified with the combined secondary vertex (CSV) algorithm [35, 36]. The jet counting for the search requires jets to be in the pseudo-rapidity range $|\eta| < 2.4$. Jets considered in the HETT analysis are required to have $p_T > 30$ GeV. The signal topologies targeted by the HPTT analysis may result in soft decay products due to the compressed mass spectrum of the produced particles. The jets considered for this analysis are therefore selected with a lower p_T threshold of 20 GeV.

Depending on the decay mode, pair production of top squarks may involve the decay of up to two on-shell top quarks and the identification of hadronically-decaying top quarks provides an important handle for suppressing most backgrounds. To this end, both methods utilize algorithms to reconstruct top quarks.

The top tagging algorithm used for the HPTT analysis identifies top quark decays with high purity, at the cost of lower signal efficiency. Top quark candidates are identified by the "CMS top tagging" (CTT) algorithm [37, 38], which makes use of jet substructure and jet mass observables in order to identify top quark decays. First, jets are reconstructed with the anti-k_T algorithm using a distance parameter of 0.8 in order to cluster the decay products of a boosted top quark into a single jet. The top candidates are then required to have large p_T (> 400 GeV) and to have their jet axis within the tracker volume ($|\eta| < 2.4$). The next step of the top reconstruction is an attempt to decompose the candidate jets into at least three subjets, where the invariant mass of these subjets is also required to be consistent with the top quark mass ($140 - 250$ GeV). The final requirement of the top identification is that the minimum invariant mass of any pair of the three highest p_T subjets found by the algorithm must exceed 50 GeV, in order to be consistent with the hadronic decay of a W boson.

The HETT analysis uses a custom top tagging algorithm designed for high efficiency, which is based on the one developed in the context of the earlier top squark search [39]. The algorithm starts with jets reconstructed using the anti-k_T algorithm with distance parameter $R = 0.4$, and tests various combinations of three jets within a large cone of radius 1.5 in η–ϕ space in order to reconstruct hadronically-decaying top quarks from resolved jets as described in Refs. [40–42]. This approach ensures high top$-$tagging efficiency at p_T below the range targeted by the boosted top quark algorithms [38]. In the HETT analysis, the efficiency of this top tagging algorithm is further improved at high p_T by using the jet mass to identify boosted scenarios in which decay products from the W boson or top quark are merged into a single jet. Details of this algorithm are presented in Section 4.1.

SM backgrounds with intrinsic $\not{E}_T$ such as leptonic $t\bar{t}$ and W+jets events are reduced by vetoing events with isolated charged leptons. Electron candidates are first reconstructed by matching clusters of energy deposits in the electromagnetic calorimeter to reconstructed tracks. A number of selection criteria based on the shower shape, track-cluster matching, and consistency between the cluster energy and track momentum are then applied for the identification of electron candidates [43]. Muon candidates are reconstructed by requiring consistent hit patterns in the tracker and muon systems [44]. The isolation of electron and muon candidates is defined as the $\sum p_T$ of PF candidates in a cone around the candidate's trajectory with a radius

$\Delta R = \sqrt{(\Delta\eta)^2 + (\Delta\phi)^2}$. The cone size depends on the lepton p_T as follows:

$$\Delta R = \begin{cases} 0.2, & p_T \leq 50 \text{ GeV} \\ \frac{10 \text{ GeV}}{p_T}, & 50 \text{ GeV} < p_T < 200 \text{ GeV} \\ 0.05, & p_T \geq 200 \text{ GeV} \end{cases} \quad (1)$$

The decrease in the cone radius for higher p_T candidates is motivated by the consideration that the decay products of more boosted heavy objects should be contained in a region defined with a smaller radius. The isolation sum is corrected for contributions originating from pileup interactions using an estimate of the pileup energy in the cone. Electron and muon candidates are considered to be isolated if their relative isolation, i.e. the ratio of the isolation sum to the candidate p_T, is less than 0.1 or 0.2 respectively. The HPTT analysis rejects events with isolated electrons or muons that have $p_T > 5$ GeV and $|\eta| < 2.4$, while the HETT analysis rejects events with isolated electrons that have $p_T > 10$ GeV and $|\eta| < 2.5$, or isolated muons that have $p_T > 10$ GeV and $|\eta| < 2.4$.

In order to further reduce the contribution from background events with low-p_T leptons originating from leptonic W boson decays, the HETT analysis places an additional veto on the presence of isolated electron or muon PF candidates using less stringent selection criteria than those described above. These tracks are required to have $p_T > 5$ GeV, $|\eta| < 2.5$, and relative track isolation less than 0.2. This is the same as the relative isolation described above except that it is only computed with charged PF candidates within a fixed cone of $\Delta R = 0.3$ around the track. In order to preserve signal efficiency the transverse mass of the track-$\not{E}_T$ system

$$M_T(\text{track}, \not{E}_T) = \sqrt{2 \cdot p_T^{\text{track}} \cdot \not{E}_T \cdot (1 - \cos\Delta\phi)} \ , \quad (2)$$

with p_T^{track} denoting the track p_T, and $\Delta\phi$ the azimuthal separation between the isolated track and $\vec{p}_T^{\text{miss}}$, is required to be less than 100 GeV to be consistent with a W boson decay.

Following vetoes on the presence of isolated electrons and muons, a significant fraction of the remaining SM background originates from events with hadronically-decaying tau leptons (τ_h). In order to reduce this background contribution, a veto is placed on the presence of isolated charged hadron PF candidates in the tracker volume with $p_T > 10$ GeV that are consistent with τ_h decays. The τ_h candidate-$\not{E}_T$ system is also required to have a transverse mass $M_T(\tau_h, \not{E}_T) < 100$ GeV. Candidates satisfying the selection on $M_T(\tau_h, \not{E}_T)$ in the case of the HETT analysis are categorized as being isolated if their relative track isolation is less than 0.1. In order to improve the discrimination between signals with low Δm and the hadronic tau background, the isolation requirement applied in the case of the HPTT analysis is based on a discriminant obtained from a multi-variate boosted decision tree (BDT) trained to distinguish the characteristics of charged hadrons originating from τ_h decays from other particles. The BDT input variables include the charged and total isolation sums within various ΔR cones around the candidate, distances in ΔR to the closest charged PF candidate and the jet containing the τ_h candidate, and the CSV value of that jet. The τ_h candidates are also required to be consistent with the primary vertex by requiring a longitudinal impact parameter less than 0.2 cm.

A summary of the object definitions used in the two analyses is tabulated in Table 1.

Table 1: Summary of the object definitions used in the HPTT and HETT analyses. The object definitions are detailed in the text.

Object	HPTT analysis	HETT analysis
Jets	anti-k_T (0.4) $p_T > 20\,GeV$, $\|\eta\| < 2.4$	anti-k_T (0.4) $p_T > 30\,GeV$, $\|\eta\| < 2.4$
b jets	$p_T > 20\,GeV$, $\|\eta\| < 2.4$	$p_T > 30\,GeV$, $\|\eta\| < 2.4$
e/μ veto	$p_T > 5\,GeV$, $\|\eta\| < 2.4$	$p_T > 10\,GeV$, $\|\eta_{e(\mu)}\| < 2.5(2.4)$
e/μ track veto	–	$p_T > 5\,GeV$, $\|\eta\| < 2.5$
τ_h track veto	$p_T > 10\,GeV$, $\|\eta\| < 2.4$ (BDT-based)	$p_T > 10\,GeV$, $\|\eta\| < 2.5$
Top reconstruction	anti-k_T (0.8) jets $p_T > 400\,GeV$, $\|\eta\| < 2.4$	anti-k_T (0.4) jets $p_T > 30\,GeV$, $\|\eta\| < 5$

2.2 Event simulation

Monte Carlo (MC) simulations of event samples are used to study the properties of the SM background processes and signal models. The MADGRAPH5 generator [45] is used to simulate events originating from $t\bar{t}$, W+jets, Z +jets, γ+jets and QCD multijet processes and from top squark pair production based on leading order (LO) NNPDF3.0 [46] parton distribution functions (PDFs). Single-top events produced in the tW channel are generated with POWHEG v1.0 [47–50], and rare SM processes such as $t\bar{t}Z$ and $t\bar{t}W$ using the MADGRAPH5_AMC@NLO program [51]. Next-to-leading order (NLO) NNPDF3.0 PDFs are used in both cases. The parton showering and hadronization is simulated with PYTHIA8.1 [52]. A GEANT4-based model [53] is used to simulate the response of the CMS detector in the case of the SM background. The CMS fast simulation package [54] is used in the case of signal samples and is verified to provide results that are consistent with those obtained from the full GEANT4-based simulation. Event reconstruction is performed in the same manner as for collision data. A nominal distribution of pileup interactions is used when producing the simulated samples. The samples are then reweighted in order to match the pileup profile observed in the collected data. The signal production cross sections are calculated using NLO plus next-to-leading logarithm (NLL) calculations [55]. The most precise available cross section calculations are used to normalize the SM simulated samples, corresponding to next-to-next-to-leading order (NNLO) accuracy in most cases.

In cases where the simulation does not adequately describe the data, correction factors are applied to account for the observed discrepancies. Differences in the efficiencies for selecting isolated leptons between simulation and data are measured in $Z \to \ell\ell$ events in the case of electrons and muons and in a $t\bar{t}$-enriched sample for hadronic taus. The observed deviations are accounted for in the form of corrections to the simulation, and the corresponding uncertainties are propagated to the predicted SM yields in the search regions. Correction factors and uncertainties based on measurements of b tagging performance in data and simulation [56] are also applied. They are parameterized by jet kinematics and flavor. An additional uncertainty related to the pileup reweighting procedure is applied to the simulation.

The top tagging efficiency and mis-identification rate of the CTT algorithm used in the HPTT analysis are measured in data and compared to the expectation from simulation. The tagging efficiency is estimated in a sample dominated by semi-leptonic $t\bar{t}$ events that are selected using a single-muon trigger. The muon is required to have $p_T > 30$ GeV and $|\eta| < 2.1$. To suppress other backgrounds, at least one b-tagged jet in the same hemisphere as the muon is required. The top candidate is required to lie in the hemisphere opposite to the muon. The contamination

from QCD multijet events is reduced to negligible levels by requiring $\not{E}_T > 50$ GeV. The efficiency estimated in simulation agrees with the measured efficiency within 10%, which is assigned as an uncertainty.

The CTT mis-identification rate of jets not originating from a top quark decay is measured in a data sample and compared with the corresponding rate in simulation. The sample is selected by a trigger with $H_T > 1$ TeV, where H_T is the scalar sum of the p_T of the jets in the event. In addition to the selection on H_T, the $\not{E}_T$ is required to exceed 200 GeV. The mis-identification rate in simulation is observed to be 30% higher than in data. The simulation is corrected for this discrepancy, and a 10% uncertainty is assigned.

The performance of the HETT is validated using a tag-and-probe inspired technique in a semi-leptonic $t\bar{t}$-enriched control region. The tagger efficiency calculated in this control region agrees well with that calculated in $t\bar{t}$ MC simulation and a flat 5% systematic uncertainty on the top quark yields is applied to cover residual differences. The efficiency calculations are discussed in more detail in Section 4.

3 The HPTT analysis

The design of the HPTT analysis is characterized by the categorization of events into exclusive search regions based on selections on kinematic variables related to jets and $\not{E}_T$. In addition, the CTT algorithm is utilized to increase the search sensitivity to signal models in which top squarks decay via on-shell top quarks. The estimation of the main backgrounds in the search regions is obtained using dedicated data control samples. The background prediction method is validated in data samples with similar characteristics to the search sample.

3.1 Event selection and categorization

The event sample used for this analysis is recorded using a trigger that requires the presence of two or more energetic jets within the tracker acceptance and a selection on $\not{E}_T$. In order to be nearly fully efficient with respect to the trigger criteria, events selected offline are required to have at least two jets with $p_T > 75$ GeV, $|\eta| < 2.4$ and $\not{E}_T > 250$ GeV. The following additional criteria define the "baseline selection" of the search sample:

- No isolated electron or muon candidates with $p_T > 5$ GeV, $|\eta| < 2.4$
- No isolated τ_h candidates with $p_T > 10$ GeV, $|\eta| < 2.4$ and $M_T(\tau_h, \not{E}_T) < 100$ GeV
- $N_j \geq 5$, where N_j denotes the number of jets with $p_T > 20$ GeV, $|\eta| < 2.4$
- $N_b^l \geq 2$, where N_b^l denotes the number of jets satisfying the "loose" working point of the CSV algorithm, with efficiency $\sim 90\%$
- $N_b \geq 1$, where N_b denotes the number of jets satisfying the "medium" working point of the CSV algorithm, with efficiency ranging between $60 - 70\%$
- $\text{Min}[|\Delta\phi(\not{E}_T, j_1)|, |\Delta\phi(\not{E}_T, j_2)|, |\Delta\phi(\not{E}_T, j_3)|, |\Delta\phi(\not{E}_T, j_4)|] \equiv \Delta\phi_{1234} > 0.5$, where j_1, j_2, j_3, j_4 are the four leading jets in p_T

Missing energy is generated in QCD multijet events through jet p_T mis-measurement, and is typically aligned with one of the leading jets in the event. Therefore, the requirements on the $|\Delta\phi|$ between the four leading jets and $\not{E}_T$ are placed in order to reduce the contribution of the QCD multijet background to a sub-dominant level.

After imposing the baseline selection requirements, a subdivision of the search sample into event categories based on kinematic observables related to jets and $\not{E}_T$ improves the power

of the analysis to discriminate between the remaining SM background and signal. The dominant sources of SM background are $\mathrm{t\bar{t}}$, W+jets, and Z+jets events. The contribution from $\mathrm{t\bar{t}}$ and W+jets processes arises from events with W bosons decaying leptonically in which the charged lepton is outside the kinematic acceptance or evades identification by the lepton vetoes. Large $\not{E}_\mathrm{T}$ can be generated by the associated neutrino, allowing such events to enter the search regions. This background will be collectively referred to as the "lost lepton" (LL) background. Contributions arising from $\mathrm{t\bar{t}W}$ and single-top processes also enter this category, but with much smaller importance. Another category of background originates from events with a Z boson produced in association with jets. Such events can enter the search regions when the Z boson decays to neutrinos, resulting in a significant amount of missing energy.

In $\mathrm{t\bar{t}}$ events with a lost lepton, the transverse mass of $\not{E}_\mathrm{T}$ and the b quark from the same top decay as the missed lepton has a kinematic end point at the mass of the top quark. The observable $M_\mathrm{T}(\mathrm{b}_{1,2}, \not{E}_\mathrm{T})$, is defined as

$$M_\mathrm{T}(\mathrm{b}_{1,2}, \not{E}_\mathrm{T}) \equiv \mathrm{Min}[M_\mathrm{T}(\mathrm{b}_1, \not{E}_\mathrm{T}), M_\mathrm{T}(\mathrm{b}_1, \not{E}_\mathrm{T})] \ , \tag{3}$$

where $\mathrm{b}_1, \mathrm{b}_2$ are the two selected b-tagged jets with the highest values of the CSV discriminator. Imposing a minimum requirement of 175 GeV on $M_\mathrm{T}(\mathrm{b}_{1,2}, \not{E}_\mathrm{T})$ reduces a significant portion of the $\mathrm{t\bar{t}}$ background, as seen in Fig. 2. However, the requirement of high $M_\mathrm{T}(\mathrm{b}_{1,2}, \not{E}_\mathrm{T})$ results in a loss in signal efficiency for signal models with small Δm between the $\tilde{\mathrm{t}}$ and $\tilde{\chi}_1^0$. In order to benefit from the separation power provided by this variable, two search categories are defined, one with $M_\mathrm{T}(\mathrm{b}_{1,2}, \not{E}_\mathrm{T}) \geq 175$ GeV taking advantage of the reduction of the $\mathrm{t\bar{t}}$ background with respect to signal models with large Δm in the high $M_\mathrm{T}(\mathrm{b}_{1,2}, \not{E}_\mathrm{T})$ category, and one with $M_\mathrm{T}(\mathrm{b}_{1,2}, \not{E}_\mathrm{T}) < 175$ GeV in order to retain the statistical power of the low $M_\mathrm{T}(\mathrm{b}_{1,2}, \not{E}_\mathrm{T})$ category for signal models with low Δm.

Signal events with hadronically decaying top quarks should have at least six jets in the final state. Additional jets may be produced through initial state radiation (ISR). The jet multiplicity is lower for the semi-leptonic $\mathrm{t\bar{t}}$ background, as well as for the other backgrounds remaining after the baseline selection. A requirement of higher reconstructed jet multiplicity therefore improves the discrimination of signal events from the SM background. Two regions in jet multiplicity are considered for the analysis, a high N_j region (≥ 7 jets) that benefits from this improved discrimination and a medium N_j region ($5-6$ jets) to preserve signal events with fewer reconstructed jets. The high N_j region in conjunction with the low threshold on the p_T of the selected jets is particularly designed to target signal models with soft decay products in the final state.

In the high $M_\mathrm{T}(\mathrm{b}_{1,2}, \not{E}_\mathrm{T})$ category, requiring at least one reconstructed top ($N_\mathrm{t} \geq 1$) ensures a high purity selection of signal events with boosted top quarks at the cost of signal efficiency. In order to benefit from this high-purity region without giving up on signal events that would enter the $N_\mathrm{t} = 0$ region, both regions are used for the final signal extraction. Subdividing each N_t region by the number of identified b-jets provides even greater discrimination of signal from background. Since there are relatively few events in the $N_\mathrm{t} \geq 1$ category, the sub-categorization in N_j is not performed for these events because it brings no additional gain after the N_b subdivision.

The event categorization in $M_\mathrm{T}(\mathrm{b}_{1,2}, \not{E}_\mathrm{T})$, N_j, N_b, and N_t is summarized in Table 2. In each of these categories, $\not{E}_\mathrm{T}$ is used as the final discriminating variable to characterize and distinguish a potential signal from the SM background. The following $\not{E}_\mathrm{T}$ regions are defined in each category: $[250, 300)$, $[300, 400)$, $[400, 500)$, $[500, 600)$, and $[600, \infty)$ GeV. The analysis is thus carried

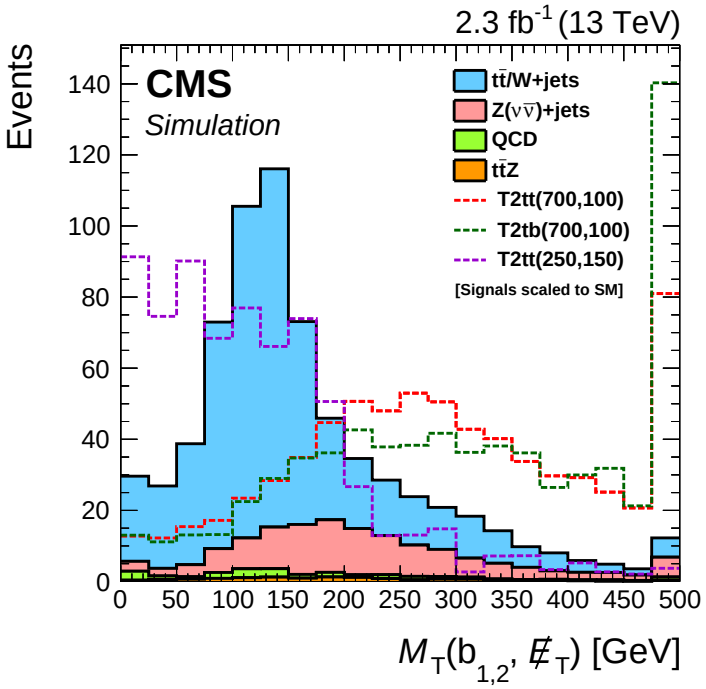

Figure 2: The $M_{\mathrm{T}}(\mathrm{b}_{1,2}, \not{E}_{\mathrm{T}})$ distribution after the HPTT analysis baseline selection, normalized to an integrated luminosity of 2.3 fb^{-1}. The expected signal yields are normalized to the total SM background expectation to facilitate a comparison of the shapes of the signal and background distributions.

out in a total of 50 disjoint regions.

Table 2: Categorization in $M_{\mathrm{T}}(\mathrm{b}_{1,2}, \not{E}_{\mathrm{T}})$, N_{j}, N_{b}, and N_{t} used to define the search regions for the HPTT analysis. Events in each category are further separated into the following $\not{E}_{\mathrm{T}}$ regions: $[250, 300)$, $[300, 400)$, $[400, 500)$, $[500, 600)$, and $[600, \infty)$ GeV, resulting in 50 disjoint search regions.

<table>
<tr><td colspan="2">$M_{\mathrm{T}}(\mathrm{b}_{1,2}, \not{E}_{\mathrm{T}}) < 175$ GeV</td><td colspan="2">$M_{\mathrm{T}}(\mathrm{b}_{1,2}, \not{E}_{\mathrm{T}}) \geq 175$ GeV</td></tr>
<tr><td>$N_{\mathrm{b}} = 1$</td><td>$N_{\mathrm{b}} \geq 2$</td><td>$N_{\mathrm{b}} = 1$</td><td>$N_{\mathrm{b}} \geq 2$</td></tr>
<tr><td rowspan="3">$5 \leq N_{\mathrm{j}} \leq 6$</td><td rowspan="3">$5 \leq N_{\mathrm{j}} \leq 6$</td><td colspan="2">$N_{\mathrm{t}} = 0$</td></tr>
<tr><td>$5 \leq N_{\mathrm{j}} \leq 6$
$N_{\mathrm{j}} \geq 7$</td><td>$5 \leq N_{\mathrm{j}} \leq 6$
$N_{\mathrm{j}} \geq 7$</td></tr>
<tr><td colspan="2">$N_{\mathrm{t}} \geq 1$</td></tr>
<tr><td>$N_{\mathrm{j}} \geq 7$</td><td>$N_{\mathrm{j}} \geq 7$</td><td>$N_{\mathrm{j}} \geq 5$</td><td>$N_{\mathrm{j}} \geq 5$</td></tr>
</table>

3.2 Estimation of the lost lepton background

The LL background is estimated from the single-lepton control sample, selected using the same trigger as for the search sample, and consisting of events that have at least one lepton obtained by inverting the e/μ-veto criteria. Studies in simulation indicate that the event kinematics for different lepton flavors are similar enough to allow us to estimate them collectively from the same control sample. Potential signal contamination is suppressed by requiring $M_{\mathrm{T}}(\ell, \not{E}_{\mathrm{T}}) < 100$ GeV. If there is more than one lepton satisfying the selection criteria, the lepton used to determine $M_{\mathrm{T}}(\ell, \not{E}_{\mathrm{T}})$ is chosen randomly. After requiring $N_{\mathrm{b}} \geq 1$, the shape of the

$\not\!\!E_T$ distribution originating from LL processes is independent of N_b, and therefore the single-lepton control sample is integrated in N_b. The events selected in the single-lepton control sample are further subdivided using the same selection on the search variables: $M_T(b_{1,2}, \not\!\!E_T)$, N_j, N_t and $\not\!\!E_T$, as in the search sample. These regions generally have 2-4 times more events than the corresponding search regions.

The estimation of the LL background in each search region is based on the event count in data, $N_{data}(1l)$, in the corresponding single-lepton control region. The event count is translated to the search region by means of a transfer factor obtained from simulation. The transfer factor, TF_{LL}, is defined as

$$TF_{LL} = \frac{N_{MC}(0l)}{N_{MC}(1l)} \ , \tag{4}$$

where $N_{MC}(0l)$ and $N_{MC}(1l)$ are the simulated LL background yields in the corresponding zero- and single-lepton regions, respectively. The formula for the LL background prediction is thus:

$$N_{pred}^{LL} = TF_{LL} \cdot N_{data}(1l), \tag{5}$$

The contamination of non-LL processes in the single-lepton control regions is found to be negligible in simulation.

In order to improve the statistical power of the estimation, control regions with $N_t \geq 1$ are integrated in $\not\!\!E_T$, since the data-to-simulation ratios ($N_{data}(1l)/N_{MC}(1l)$) in regions with similar kinematics (i.e. $M_T(b_{1,2}, \not\!\!E_T) > 175$, $N_t = 0$) show no evidence of dependence on $\not\!\!E_T$. The systematic uncertainty in the extrapolation in each $\not\!\!E_T$ region is based upon the relative statistical uncertainty of the data-to-simulation ratios obtained in the same $\not\!\!E_T$ region in events with $M_T(b_{1,2}, \not\!\!E_T) > 175$ and $N_t = 0$.

Figure 3 displays a comparison of the $\not\!\!E_T$ distribution in simulated and data events in two event categories in the single-lepton sample.

The transfer factors are corrected for differences observed between simulation and data. In particular, correction factors for lepton selection efficiencies are applied in order to ensure a good description of both the zero- and single-lepton samples. The uncertainties in the measurements of the lepton efficiency correction factors lead to a systematic uncertainty of up to 7% in TF_{LL}. An additional source of bias in the prediction may arise from a possible difference between data and simulation in the background composition, which is assessed by independently varying the cross sections of W+jets and $t\bar{t}$ processes by 20%. The effect of these variations on the transfer factors is up to 11%. Uncertainties of 10% are associated with measurements of differences in the top tagging efficiency and mis-identification rate between data and simulation. The dominant uncertainty associated with the prediction is the result of the limited statistics of the control regions. The statistics of the simulated samples also affect the uncertainty on the prediction via the transfer factors.

3.3 Estimation of the $Z \to \nu\nu$ background

The estimation of the $Z \to \nu\nu$ background combines information from Z+jets, with $Z \to \ell\ell$, and γ+jets samples. The former, referred to as the $Z \to \ell\ell$ sample, is utilized to measure the normalization of the $Z \to \nu\nu$ background in different ranges of N_b, while the much higher

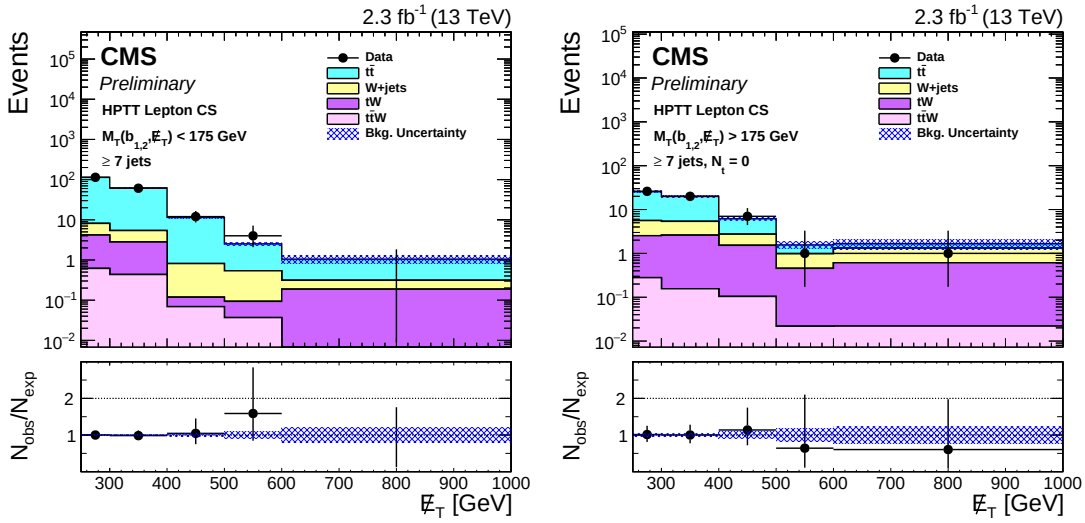

Figure 3: Comparison of the $\not\!\!E_T$ distribution for two event categories in the single-lepton sample for the HPTT analysis. The plot on the left is for events with $M_T(b_{1,2}, \not\!\!E_T) < 175$ GeV and $N_j \geq 7$, whereas the plot on the right is for events with $M_T(b_{1,2}, \not\!\!E_T) > 175$ GeV, $N_t = 0$ and $N_j \geq 7$. Data and simulation are represented by the black points and stacked histograms, respectively. The error bars on the ratio of observed data to simulation correspond to the statistical uncertainty in the data. and the shaded blue band represents the statistical uncertainty on the simulation. The simulation is normalized to the data.

yields of the γ+jets sample are exploited to extract corrections to the search region variable distribution shapes. The $Z \to \ell\ell$ sample is obtained using di-electron and di-muon triggers. The leading lepton is required to have $p_T > 20$ GeV while the trailing lepton must satisfy $p_T > 15$ and 10 GeV for electrons and muons, respectively. The γ+jets sample is collected by means of a single photon trigger where photons with $p_T > 180$ GeV are selected. The di-lepton or photon systems are added vectorially to $\vec{p}_T^{\,miss}$ in each event of the corresponding data samples. The modified $\not\!\!E_T$, denoted by $\not\!\!E_T^{\ell\ell}$ and $\not\!\!E_T^{\gamma}$ for the $Z \to \ell\ell$ and γ+jets processes respectively, is used to calculate related kinematic variables.

The prediction of the $Z \to \nu\nu$ background is given by:

$$N_{pred}^{Z\to\nu\nu} = N_{MC}^{Z\to\nu\nu} \cdot R_Z \cdot S_\gamma \tag{6}$$

where, $N_{MC}^{Z\to\nu\nu}$ is the expected number of $Z \to \nu\nu$ events obtained from simulation, R_Z is the normalization factor, and S_γ accounts for shape corrections.

The factor R_Z is calculated by comparing the observed and expected $Z \to \ell\ell$ yields after applying a relaxed version of the baseline selection. In particular, the requirement on the azimuthal angle between the leading jets and $\not\!\!E_T^{\ell\ell}$ is removed after confirming that this does not bias the result, and the requirement on $\not\!\!E_T$ is relaxed from a threshold of 250 GeV to a threshold of 100 GeV. To increase the purity of the $Z \to \ell\ell$ sample, the di-lepton invariant mass is required to lie within the Z-mass window ($80 < M_{ll} < 100$ GeV). The normalization of the non-negligible $t\bar{t}$ contamination is estimated in the region outside the Z-mass window ($20 < M_{ll} < 80$ or $M_{ll} > 100$ GeV) and taken into account in the calculation of R_Z.

To account for potential effects related to heavy flavor production, R_Z is calculated separately for different N_b requirements. The measured values are: $R_Z(N_b = 1) = 0.94 \pm 0.12 \pm 0.06$ and $R_Z(N_b \geq 2) = 0.84 \pm 0.19 \pm 0.01$. The first uncertainty is due to the statistics of the data and

simulated samples, whereas the second uncertainty accounts for the $\not\!\!E_T$ extrapolation.

The quantity S_γ is the shape correction factor related to the modeling of the kinematics of $Z \to \nu\nu$ events. It is calculated via a comparison of the $\not\!\!E_T^\gamma$ distributions of γ+jets events in simulation and data. The simulation is normalized to the number of events seen in data after applying the baseline selection. To suppress potential signal contamination, only events with $\not\!\!E_T < 200\,\text{GeV}$ are considered. The S_γ factor is estimated separately for each search region, to account for any potential mis-modeling of the observables $M_T(b_{1,2}, \not\!\!E_T)$, N_j, $\not\!\!E_T^\gamma$ and N_t in simulation. Since no statistically significant dependence of $\not\!\!E_T^\gamma$ on N_b is observed, the γ+jets sample is integrated over N_b to improve the statistical power of the correction.

The γ+jets data control sample has contributions from three main components: prompt photons produced directly, via fragmentation, and fake photons. The prompt photon purity is measured by performing a maximum likelihood fit to data using the photon isolation quantity as a discriminating variable, with different templates describing the distribution of the photon isolation for the prompt and fake-photon components [57]. The purity measured in data is found to be in good agreement with the expectation from simulation. Additionally, the impact of varying the fraction of fake photons or those produced via fragmentation by 50% results in less than a 5% bias in the $\not\!\!E_T$ distribution of the predicted $Z \to \nu\nu$ background. The fractions of the three different components are therefore estimated using simulation.

The γ+jets sample can also be contaminated with $t\bar{t}\gamma$ events. The contribution of this process is estimated using simulation, after verifying that this produces no significant bias in the prediction.

The two major sources of uncertainty in the $Z \to \nu\nu$ prediction are the statistical uncertainty in the γ+jets control sample and the uncertainty in R_Z. The statistical uncertainty of simulated samples ranges up to about 50% in both the search regions and the γ+jets control regions. The jet energy scale uncertainty ranges up to 34% in some search regions. An uncertainty of 10% is assigned to the prediction to account for differences in the top mis-identification rates between simulation and data.

Figure 4 compares the normalized $\not\!\!E_T^\gamma$ distributions for γ+jets events in data and simulation in two event categories. The data to simulation ratios in the various $\not\!\!E_T^\gamma$ bins are the S_γ weights used to correct the $Z \to \nu\nu$ simulated sample. The weights range from 0.2 to 1.8 depending on the search region.

3.4 Estimation of the QCD multijet background

The background stemming from QCD multijet processes is estimated utilizing a data control sample selected using the same trigger as for the search sample and enriched in QCD events by requiring $\text{Min}[|\Delta\phi(\not\!\!E_T, j_1)|, |\Delta\phi(\not\!\!E_T, j_2)|, |\Delta\phi(\not\!\!E_T, j_3)|] \equiv \Delta\phi_{123} < 0.1$. The observation in this control sample is translated to a prediction in the search sample by correlating the expected QCD multijet events satisfying $\Delta\phi_{123} < 0.1$ and $\Delta\phi_{1234} > 0.5$ using simulation. The estimation is carried out in each search category. Since the shapes of key observables show little dependence on N_b, the QCD control sample is integrated over N_b to improve the statistical precision of the estimation.

The main source of QCD events populating the search sample is due to severe mis-measurement of the transverse momentum of one or more jets in the event. Therefore, the correct modeling of jet mis-measurement in simulation is an important component of the QCD prediction. The level of mis-measurement in an event is parameterized by the jet response of the most mis-measured jet, which is the jet with the greatest absolute difference between reconstructed and

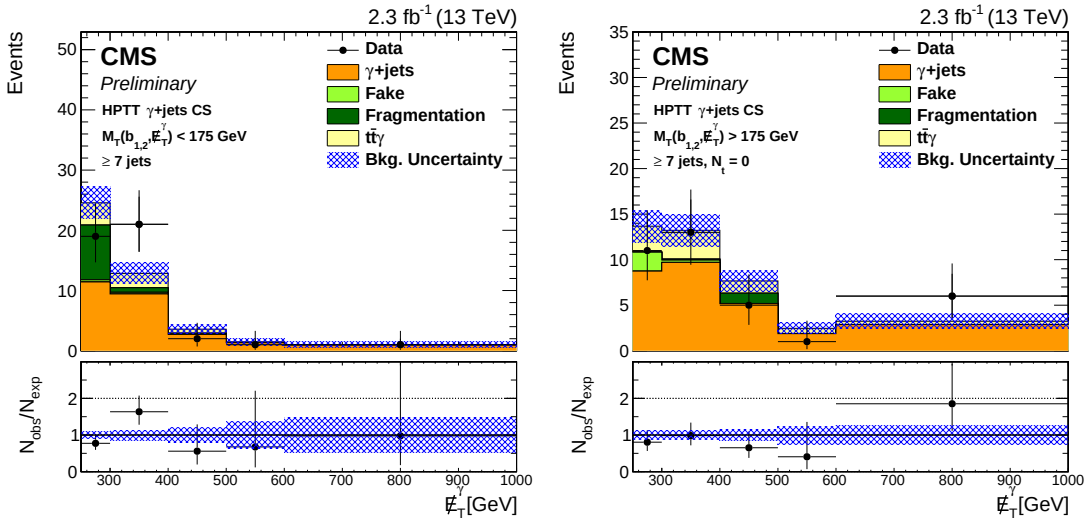

Figure 4: Comparison of the normalized $\not{E}_{\mathrm{T}}^{\gamma}$ distributions in the γ+jets sample in data and simulation, in two of the control regions for the HPTT analysis. The plot on the left is for events with $M_{\mathrm{T}}(\mathrm{b}_{1,2}, \not{E}_{\mathrm{T}}) < 175$ GeV and $N_{\mathrm{j}} \geq 7$, whereas the plot on the right is for events with $M_{\mathrm{T}}(\mathrm{b}_{1,2}, \not{E}_{\mathrm{T}}) > 175$ GeV, $N_{\mathrm{t}} = 0$ and $N_{\mathrm{j}} \geq 7$. The data to simulation ratios in the various $\not{E}_{\mathrm{T}}^{\gamma}$ bins are the S_{γ} weights used to correct the $\mathrm{Z} \to \nu\nu$ simulation sample.

generated p_{T}. The jet response, r_{jet}, is defined as the ratio of the reconstructed jet p_{T} to the generated jet p_{T} before reconstruction and without including the loss of visible momentum due to neutrinos. However, r_{jet} cannot be defined in data and therefore mis-measurement correction factors are derived with the $r_{\mathrm{jet}}^{\mathrm{pseudo}}$ of the jet closest in $|\phi|$ to $\vec{p}_{\mathrm{T}}^{\,\mathrm{miss}}$. The observable $r_{\mathrm{jet}}^{\mathrm{pseudo}}$ is defined as the ratio of a jet's p_{T} to the vector sum of its momentum and $\vec{p}_{\mathrm{T}}^{\,\mathrm{miss}}$. The $r_{\mathrm{jet}}^{\mathrm{pseudo}}$ distribution is compared in data and simulation and correction factors are extracted based on the r_{jet} and the flavor of the most mis-measured jet. The correction factors range between $0.44 - 1.13$. These correction factors are applied on an event by event basis.

QCD multijet events have a large cross section. As a result, the simulated QCD multijet sample does not have the same luminosity as the collected data and the simulated event yields in some regions are too low to obtain a background estimation or result in an estimate with large statistical uncertainty. The r_{jet} distribution is therefore extrapolated in order to increase the statistical power of the sample. Technically, this is done by constructing a "smeared" QCD multijet sample by using each event from the original sample to produce multiple smeared events. A smeared event is created by randomly assigning r_{jet} values to the leading two jets, ranked by true jet p_{T}, and then recalculating jet momenta, $\not{E}_{\mathrm{T}}$, and all other event variables. The r_{jet} values are sampled from inclusive r_{jet} distributions binned in both generated jet p_{T} and jet flavor. Each original event is smeared 100 times and the statistical uncertainty on evaluated quantities is estimated with a bootstrapping procedure [58] that utilizes 50 pseudo experiments.

Figure 5 shows the data and simulated yields in both the most and the least populated control regions. The r_{jet} scale factors improve the agreement between data and simulation, with the corrected simulation generally agreeing with data.

3.5 Estimation of the $\mathrm{t\bar{t}Z}$ background

The $\mathrm{t\bar{t}Z}$ contributions are generally small, but they are non-negligible in some search regions that require large $\not{E}_{\mathrm{T}}$ and $N_{\mathrm{t}} \geq 1$. While this is a relatively rare process, it has a final state

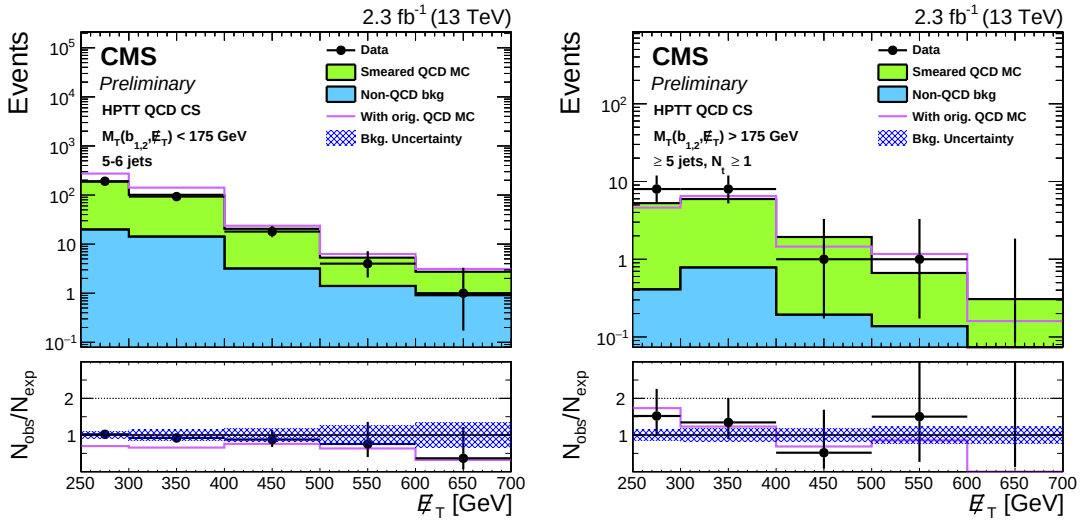

Figure 5: Data and simulated yields in the $M_{\mathrm{T}}(\mathrm{b}_{1,2}, \not{E}_{\mathrm{T}}) < 175\,\mathrm{GeV}$, $5-6$ jet (left) and the $M_{\mathrm{T}}(\mathrm{b}_{1,2}, \not{E}_{\mathrm{T}}) > 175\,\mathrm{GeV}$, $N_{\mathrm{t}} \geq 1$ (right) HPTT QCD control regions. The line labeled "Observed" displays data yields. The stacked histogram labelled "Non-QCD bkg" shows the SM yields of all processes other than QCD, as determined with the dedicated background estimation methods. The other stacked histogram, labelled "Smeared QCD MC," shows the smeared QCD multijet simulation yields. The line labelled "With orig. QCD MC" is the simulation without smearing or the r_{jet} correction. Error bars on the ratio of the observed to expected event yields in the bottom pane include only statistical uncertainties on the data yields. The filled band in this pane represents the relative uncertainty on the expected event yields, including the statistical uncertainty on the QCD MC yields and the systematic uncertainty due to contamination from non-QCD SM backgrounds.

very similar to that of signal when the Z boson decays to neutrinos and both top quarks decay hadronically. The $\mathrm{t\bar{t}Z}$ prediction is obtained from simulation. A 30% uncertainty is assigned to the $\mathrm{t\bar{t}Z}$ cross section, based on the 8 TeV CMS measurement [59]. Additional uncertainties are assigned based on the effects of variations of the factorization and renormalization scales used in the simulation by a factor of 2 [60, 61] on the acceptance for this process in each search region. Uncertainties related to the parton distribution functions and the value of the strong coupling constant are also considered. These theoretical uncertainties on the simulation generally vary from 2-25%. The 2.7% uncertainty on the integrated luminosity measured by CMS directly affects the $\mathrm{t\bar{t}Z}$ prediction. Uncertainties related to the modeling of the b tagging efficiency, jet energy scale, pileup and lepton vetoes in simulation are also assigned to the prediction. Finally, the statistical uncertainty of the simulation sample is taken into account.

3.6 Validation of the analysis in data

In order to test and validate the background prediction, the entire analysis is carried out in data samples that are selected with the same selection as the search sample except for orthogonal requirements on either N_{j}, $\not{E}_{\mathrm{T}}$ or N_{b}. The first validation sample consists of events with $2 \leq N_{\mathrm{j}} \leq 4$, designed to test the background prediction in different $\not{E}_{\mathrm{T}}$ and N_{b} regions. The background estimation in different N_{j} regions is validated in a data sample with events satisfying $\not{E}_{\mathrm{T}} \in [200, 250)\,\mathrm{GeV}$. The estimation of the $\mathrm{Z} \to \nu\nu$ background is tested in a validation sample consisting of events with $N_{\mathrm{b}} = 0$. The data agree well with the estimated background yields within statistical uncertainties in all three validation samples. The comparison of the

background prediction with the observed data in the $N_b = 0$ sample is shown in Fig. 6.

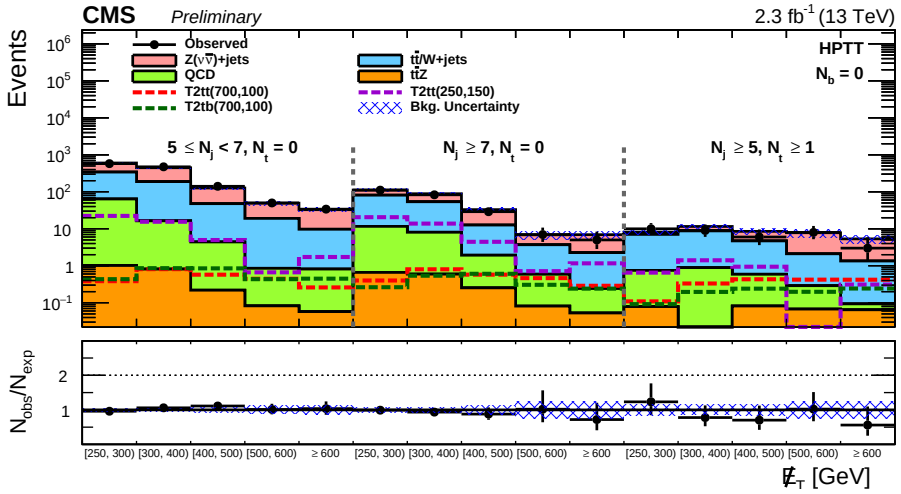

Figure 6: Test of the background prediction method in the $N_b = 0$ validation region for the HPTT analysis. The data agree well with the estimated background yields within statistical uncertainties.

3.7 Results

Figure 7 shows the observed events in each of the search region bins, as well as the predicted SM background yields based on the background estimation methods discussed in Sections 3.2-3.5. Expected yields are also shown for two benchmark signal models in the T2tt scenario. The predicted SM background yields and observed events in each search region are tabulated in Table 3. No statistically significant deviation from the SM prediction is observed.

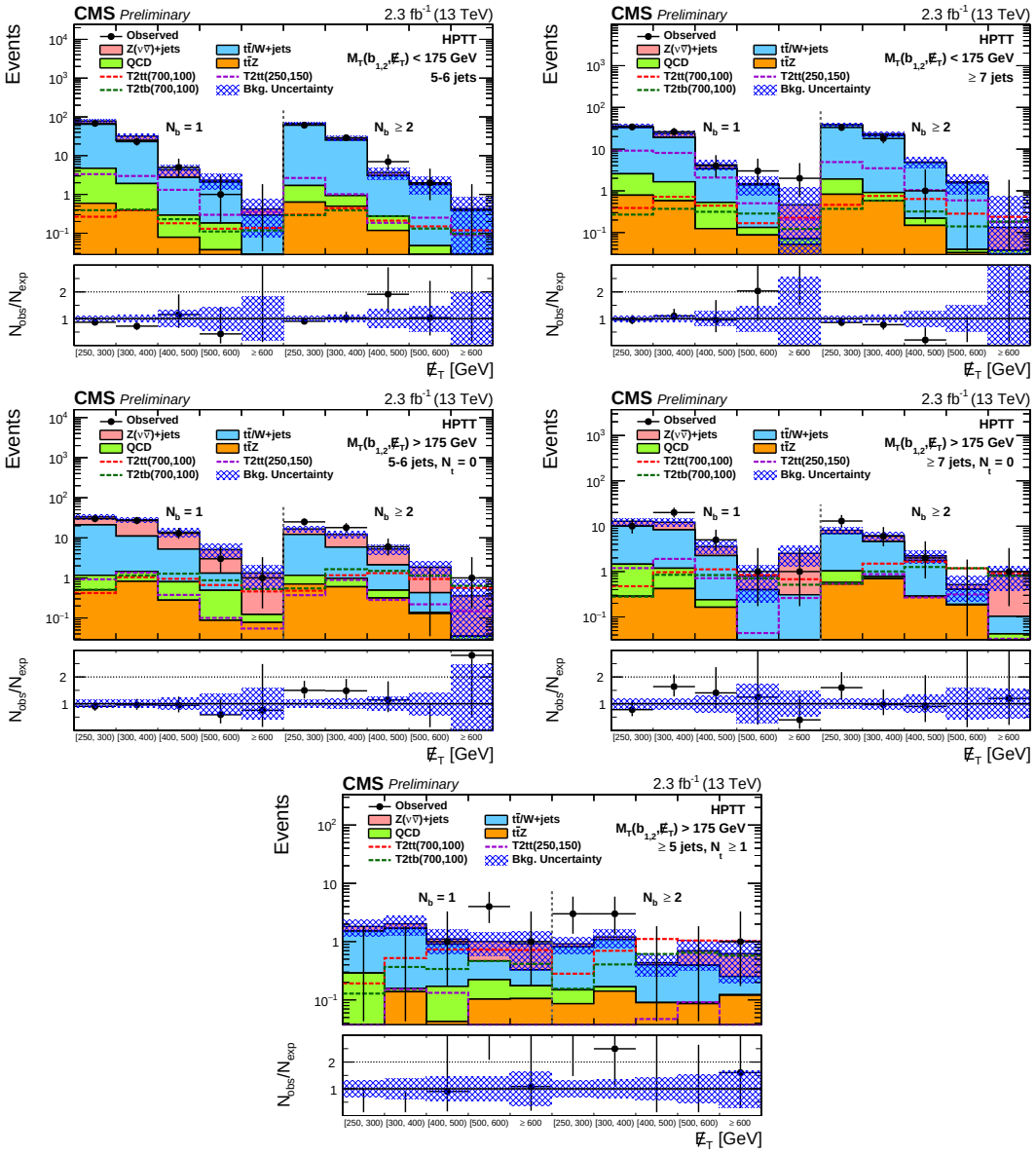

Figure 7: Observed events and estimated SM background and signal yields for the HPTT analysis search regions: $M_{\mathrm{T}}(\mathrm{b}_{1,2}, \not{E}_{\mathrm{T}}) < 175$ GeV, $N_{\mathrm{j}} \in [5,6]$ (upper left), $M_{\mathrm{T}}(\mathrm{b}_{1,2}, \not{E}_{\mathrm{T}}) < 175$ GeV, $N_{\mathrm{j}} \geq 7$ (upper right), $M_{\mathrm{T}}(\mathrm{b}_{1,2}, \not{E}_{\mathrm{T}}) > 175$ GeV, $N_{\mathrm{t}} = 0, N_{\mathrm{j}} \in [5,6]$ (middle left), $M_{\mathrm{T}}(\mathrm{b}_{1,2}, \not{E}_{\mathrm{T}}) > 175$ GeV, $N_{\mathrm{t}} = 0, N_{\mathrm{j}} \geq 7$ (middle right), $M_{\mathrm{T}}(\mathrm{b}_{1,2}, \not{E}_{\mathrm{T}}) > 175$ GeV, $N_{\mathrm{t}} \geq 1, N_{\mathrm{j}} \geq 5$ (bottom row). The first 5 bins in each plot correspond to $\not{E}_{\mathrm{T}} \in [250,300), [300,400), [400,500), [500,600), [600,\infty)$ GeV for $N_{\mathrm{b}} = 1$, and the second 5 bins correspond to the same $\not{E}_{\mathrm{T}}$ binning for $N_{\mathrm{b}} \geq 2$. The SM background predictions shown do not include the effects of the maximum likelihood fit to the data. The ratios of the observed data to the SM prediction derived from control regions (black points, with error bars corresponding to the data statistical uncertainty), and to the expectation obtained directly from simulation (solid red line), are shown in the ratio plots. The shaded blue band represents the statistical and systematic uncertainty on the background prediction.

Table 3: Predicted yields for each background with uncertainties in each of the HPTT analysis search regions. The number of events observed in data is given in the last column.

$\not{E}_T$ [GeV]	$t\bar{t}$/W+jets	$Z \to \nu\nu$	QCD	$t\bar{t}Z$	Total SM	Data
$M_T(b_{1,2}, \not{E}_T) < 175$ GeV, $5 \leq N_j < 7$, $N_b = 1$						
250-300	60 ± 6	14 ± 3	4.1 ± 1.7	0.59 ± 0.21	79 ± 7	68
300-400	23 ± 3	7.4 ± 1.9	1.5 ± 0.8	0.39 ± 0.14	32 ± 4	23
400-500	2.5 ± 1.0	1.6 ± 0.8	0.21 ± 0.15	0.08 ± 0.04	4.3 ± 1.3	5
500-600	1.9 ± 1.0	0.25 ± 0.27	0.14 ± 0.15	0.04 ± 0.02	2.3 ± 1.0	1
>600	0.28 ± 0.31	0.13 ± 0.15	0.01 ± 0.01	<0.01	0.42 ± 0.34	0
$M_T(b_{1,2}, \not{E}_T) < 175$ GeV, $5 \leq N_j < 7$, $N_b \geq 2$						
250-300	61 ± 6	4.7 ± 1.4	1.1 ± 0.5	0.63 ± 0.22	68 ± 6	61
300-400	24 ± 3	3.0 ± 1.0	0.44 ± 0.23	0.50 ± 0.18	28 ± 4	29
400-500	2.8 ± 1.2	0.61 ± 0.33	0.16 ± 0.13	0.12 ± 0.06	3.7 ± 1.2	7
500-600	1.7 ± 0.9	0.13 ± 0.15	0.05 ± 0.06	<0.01	1.9 ± 0.9	2
>600	0.38 ± 0.41	0.04 ± 0.06	<0.01	0.01 ± 0.01	0.43 ± 0.41	0
$M_T(b_{1,2}, \not{E}_T) < 175$ GeV, $N_j \geq 7$, $N_b = 1$						
250-300	30 ± 4	3.0 ± 1.0	1.8 ± 0.6	0.79 ± 0.28	36 ± 4	34
300-400	17 ± 3	4.6 ± 1.6	1.1 ± 0.5	0.58 ± 0.21	24 ± 3	26
400-500	2.9 ± 0.9	0.82 ± 0.64	0.40 ± 0.27	0.12 ± 0.07	4.2 ± 1.1	4
500-600	1.3 ± 0.7	0.09 ± 0.11	0.05 ± 0.05	0.09 ± 0.05	1.5 ± 0.7	3
>600	<0.56	0.39 ± 0.46	0.02 ± 0.02	0.05 ± 0.03	0.46 ± 0.72	2
$M_T(b_{1,2}, \not{E}_T) < 175$ GeV, $N_j \geq 7$, $N_b \geq 2$						
250-300	36 ± 4	0.96 ± 0.38	1.1 ± 0.5	0.83 ± 0.30	38 ± 4	33
300-400	20 ± 3	2.1 ± 0.9	0.34 ± 0.19	0.58 ± 0.22	23 ± 3	18
400-500	4.5 ± 1.4	0.15 ± 0.13	0.07 ± 0.05	0.15 ± 0.07	4.9 ± 1.4	1
500-600	1.5 ± 0.8	0.09 ± 0.11	0.01 ± 0.01	0.03 ± 0.03	1.6 ± 0.8	0
>600	<0.59	0.10 ± 0.12	0.01 ± 0.01	0.03 ± 0.02	0.13 ± 0.60	0
$M_T(b_{1,2}, \not{E}_T) \geq 175$ GeV, $5 \leq N_j < 7$, $N_t = 0$, $N_b = 1$						
250-300	20 ± 3	12 ± 3	0.66 ± 0.37	0.50 ± 0.19	33 ± 5	30
300-400	9.6 ± 2.3	17 ± 4	0.63 ± 0.32	0.82 ± 0.27	28 ± 4	27
400-500	4.4 ± 1.9	8.6 ± 2.6	0.52 ± 0.35	0.28 ± 0.12	14 ± 3	13
500-600	0.82 ± 0.63	3.8 ± 1.8	0.40 ± 0.35	0.09 ± 0.06	5.1 ± 1.9	3
>600	<0.4	1.2 ± 0.7	0.05 ± 0.05	0.08 ± 0.04	1.3 ± 0.8	1
$M_T(b_{1,2}, \not{E}_T) \geq 175$ GeV, $5 \leq N_j < 7$, $N_t = 0$, $N_b \geq 2$						
250-300	11 ± 2	4.5 ± 1.4	0.45 ± 0.27	0.70 ± 0.24	17 ± 3	25
300-400	4.9 ± 1.2	6.3 ± 1.8	0.37 ± 0.23	0.60 ± 0.22	12 ± 2	18
400-500	1.6 ± 0.7	3.1 ± 1.1	0.18 ± 0.17	0.31 ± 0.12	5.3 ± 1.4	6
500-600	0.29 ± 0.24	1.4 ± 0.8	0.01 ± 0.01	0.13 ± 0.06	1.9 ± 0.8	0
>600	<0.49	0.32 ± 0.20	0.01 ± 0.02	0.02 ± 0.02	0.36 ± 0.53	1
$M_T(b_{1,2}, \not{E}_T) \geq 175$ GeV, $N_j \geq 7$ $N_t = 0$, $N_b = 1$						
250-300	8.8 ± 1.9	2.5 ± 1.0	1.2 ± 0.6	0.29 ± 0.18	13 ± 2	10
300-400	7.1 ± 1.8	3.9 ± 1.5	0.76 ± 0.46	0.42 ± 0.18	12 ± 2	20
400-500	2.0 ± 0.8	1.3 ± 0.7	0.08 ± 0.07	0.16 ± 0.09	3.6 ± 1.1	5
500-600	0.38 ± 0.40	0.40 ± 0.43	0.02 ± 0.02	<0.01	0.80 ± 0.59	1
>600	0.28 ± 0.33	2.2 ± 1.2	0.02 ± 0.03	<0.01	2.5 ± 1.2	1
$M_T(b_{1,2}, \not{E}_T) \geq 175$ GeV, $N_j \geq 7$ $N_t = 0$, $N_b \geq 2$						
250-300	5.9 ± 1.3	1.2 ± 0.5	0.46 ± 0.24	0.57 ± 0.21	8.1 ± 1.5	13
300-400	3.8 ± 1.0	1.6 ± 0.7	0.08 ± 0.06	0.70 ± 0.26	6.2 ± 1.2	6
400-500	1.5 ± 0.6	0.48 ± 0.27	0.01 ± 0.01	0.28 ± 0.12	2.2 ± 0.7	2
500-600	0.22 ± 0.25	0.11 ± 0.12	0.01 ± 0.01	0.18 ± 0.08	0.51 ± 0.29	0
>600	0.06 ± 0.07	0.73 ± 0.44	0.02 ± 0.03	0.02 ± 0.03	0.84 ± 0.45	1
$M_T(b_{1,2}, \not{E}_T) \geq 175$ GeV, $N_j \geq 5$, $N_t \geq 1$, $N_b = 1$						
250-300	1.2 ± 0.5	0.30 ± 0.25	0.26 ± 0.21	0.02 ± 0.03	1.8 ± 0.6	0
300-400	1.5 ± 0.7	0.34 ± 0.26	0.02 ± 0.01	0.14 ± 0.06	2.0 ± 0.8	0
400-500	0.73 ± 0.40	0.20 ± 0.22	0.13 ± 0.17	0.04 ± 0.05	1.1 ± 0.5	1
500-600	0.25 ± 0.22	0.54 ± 0.34	0.12 ± 0.16	0.10 ± 0.06	1.0 ± 0.4	4
>600	0.15 ± 0.33	0.59 ± 0.49	0.07 ± 0.07	0.11 ± 0.05	0.92 ± 0.60	1
$M_T(b_{1,2}, \not{E}_T) \geq 175$ GeV, $N_j \geq 5$, $N_t \geq 1$, $N_b \geq 2$						
250-300	0.66 ± 0.26	0.11 ± 0.09	0.06 ± 0.05	0.09 ± 0.05	0.92 ± 0.29	3
300-400	0.92 ± 0.39	0.12 ± 0.10	0.03 ± 0.03	0.14 ± 0.08	1.2 ± 0.4	3
400-500	0.31 ± 0.17	0.03 ± 0.04	<0.01	0.09 ± 0.06	0.43 ± 0.18	0
500-600	0.30 ± 0.30	0.30 ± 0.21	<0.01	0.09 ± 0.04	0.70 ± 0.37	0
>600	0.13 ± 0.29	0.37 ± 0.32	<0.01	0.12 ± 0.05	0.62 ± 0.43	1

4 The HETT analysis

The HETT analysis is designed for maximum sensitivity to models containing top quarks in their decay chains. The T2tt model of the SMS framework is used as a particular benchmark for optimization of this analysis. Targeting these final states with top quarks, the data are first divided into search regions based upon the number of top quarks tagged (N_t) and b-tagged jets (N_b) found in each event. The search regions are ultimately defined by further sub-division of each N_t, N_b bin in $\not{E}_T$ and M_{T2}, defined in Sec. 4.1. SM backgrounds come from processes such as QCD multijet events, Z bosons produced in association with jets (Z+jets), top quarks or W bosons produced in association with jets ($t\bar{t}/W+$jets), and smaller contributions from rare SM processes.

4.1 Top quark reconstruction and identification

The procedure to reconstruct and identify the hadronically-decaying top quarks (top tagging) presented here is similar to the one used in Ref. [39], where reconstruction of the hadronically decaying top quarks from resolved jets is performed as described in Refs. [40–42]. The top tagging algorithm is improved in this work, compared with Ref. [39], to be sensitive to boosted scenarios in which decay products from the W boson or top quark are merged into a single jet, as well as to allow tagging of more than one top quark.

The top tagging algorithm takes as input all jets that satisfy $p_T > 30\,\text{GeV}$ and $|\eta| < 5$. The jets are then clustered into triplets, subject to the following conditions; (i) Each jet lies within a cone of radius 1.5 in (η, ϕ) space, centered at the direction defined by the trijet combination. The radius requirement implies a moderate Lorentz boost of the top quark as expected for events with large $\Delta m = m_{\tilde{t}} - m_{\tilde{\chi}_1^0}$ targeted in this search. (ii) The trijet system mass ($m_{3\text{-jet}}$) must be within the range approximately 100–250 GeV, dependent on the number of top candidates found in the event. (iii) The trijet system must satisfy one of the three following criteria:

$$
\begin{aligned}
&\text{a)}\ \ 0.2 < \arctan\left(\frac{m_{13}}{m_{12}}\right) < 1.3 \ \text{ and } \ R_{\text{min}} < \frac{m_{23}}{m_{3\text{-jet}}} < R_{\text{max}}, \\
&\text{b)}\ \ R_{\text{min}}^2\left(1+\left(\frac{m_{13}}{m_{12}}\right)^2\right) < 1-\left(\frac{m_{23}}{m_{3\text{-jet}}}\right)^2 < R_{\text{max}}^2\left(1+\left(\frac{m_{13}}{m_{12}}\right)^2\right), \\
&\text{c)}\ \ R_{\text{min}}^2\left(1+\left(\frac{m_{12}}{m_{13}}\right)^2\right) < 1-\left(\frac{m_{23}}{m_{3\text{-jet}}}\right)^2 < R_{\text{max}}^2\left(1+\left(\frac{m_{12}}{m_{13}}\right)^2\right).
\end{aligned}
\tag{7}
$$

Here, m_{12}, m_{13}, and m_{23} are the dijet masses, where the jet indices 1, 2, and 3 are p_T ordered. The numerical constants have values $R_{\text{min}} = 0.85 \cdot (m_W/m_t)$ and $R_{\text{max}} = 1.25 \cdot (m_W/m_t)$, with $m_W = 80.4\,\text{GeV}$ and $m_t = 173.4\,\text{GeV}$ [62]. The top-quark tagging conditions a), b), or c) can be reduced (under certain approximations detailed in Ref. [41]) to the requirement that $m_{23}/m_{3\text{-jet}}$, $m_{12}/m_{3\text{-jet}}$, or $m_{13}/m_{3\text{-jet}}$, respectively, be consistent with the m_W/m_t ratio. Any top candidate which shares a jet with another candidate is removed, giving preference to the candidate with $m_{3\text{-jet}}$ closer to the true top mass. The remaining triplets are then counted as top-tagged objects, whose momentum four-vectors are computed as the sum of the momentum four-vectors of the constituent jets.

To further improve the efficiency of the top tagger for large top p_T, cases where W or top decay products are merged are also considered. Jets that orginate from the merged decay products of a W boson (merged W jet) or top quark (merged top jet) are identified by the requirement that the jet mass is in the 70–110 GeV or 110–220 GeV range, respectively. In case a merged top jet is found, it is added to the list of top-tagged objects. On the other hand, if a merged W boson

jet is identified, an additional jet is combined with it to form a potential top candidate. The merged W boson jet is treated as a "dijet" system in the top tagging algorithm, and $R_{\min} < m_{\text{dijet}}/m_{\text{dijet+j}} < R_{\max}$ and $100 < m_{\text{dijet+j}} < 250\,\text{GeV}$ are used as criteria to decide whether it is a good top candidate. Jets which are already included in a top-tagged jet triplet, as described above, are excluded from being considered in "dijet" + jet top candidates. Again, candidates with overlapping jets are discarded, giving preference to the candidate with $m_{\text{3-jet}}$ closer to the true top mass.

By considering not only fully resolved (three-jet) top quark decays, but also decays from boosted top quarks, manifesting themselves as one- or two-jet topologies, this custom inclusive top tagger achieves a high efficiency for tagging top quarks over a wide range of top quark p_{T}, from ∼30% at 200 GeV to close to 85% at 1 TeV. The tagging efficiency is measured using the T2tt signal model with $m_{\tilde{\text{t}}} = 850\,\text{GeV}$ and $m_{\tilde{\chi}^0_1} = 100\,\text{GeV}$ since it has a wide top quark p_{T} spectrum. A pre-selection is applied by requiring at least 4 jets with $p_{\text{T}} > 30\,\text{GeV}$ and $|\eta| < 2.4$. The top-tagged object must be matched to the hadronically decaying generator-level top quark within a cone of radius 0.4 in (η, ϕ) space. The top-tagging efficiency as a function of top quark p_{T} is shown in Fig. 8, which also includes the expected p_{T} distributions for the hadronically decaying top quark in $\text{t}\bar{\text{t}}$ events, as well as in various T2tt signal models. Since the top quark p_{T} spectrum for signal events depends strongly on $m_{\tilde{\text{t}}}$ and $\Delta m(\tilde{\text{t}}, \tilde{\chi}^0_1)$, the good tagging efficiency across the top quark p_{T} spectrum insures good acceptance for a wide range of signal models. The event mistag rate of the custom inclusive top tagger is about 30–40% for processes that do not contain hadronically decaying top quarks. These processes, as well as the $\text{t}\bar{\text{t}}$ process, are suppressed by using the stransverse mass variable M_{T2} as a complement to the top tagger.

The stransverse mass variable M_{T2} [30, 31] is an extension of the transverse mass variable that is sensitive to the pair production of heavy particles, each of which decays to an invisible particle. The M_{T2} variable is defined, for two $\tilde{\text{t}}$ particles ((1) and (2)) decaying to some visible energy and a invisible particle (χ^0_1) as:

$$M_{\text{T2}} \equiv \min_{\vec{q}^{(1)}_{\text{T}} + \vec{q}^{(2)}_{\text{T}} = \vec{p}^{\,\text{miss}}_{\text{T}}} \left[\max\{ m^2_{\text{T}}(\vec{p}^{(1)}_{\text{T}}; m^{(1)}_{\text{p}}, \vec{q}^{(1)}_{\text{T}}; m_{\tilde{\chi}^0_1}), m^2_{\text{T}}(\vec{p}^{(2)}_{\text{T}}; m^{(2)}_{\text{p}}, \vec{q}^{(2)}_{\text{T}}; m_{\tilde{\chi}^0_1}) \} \right] \tag{8}$$

where $\vec{p}^{(i)}_{\text{T}}$ and $m^{(i)}_{\text{p}}$ are the transverse momentum and mass of the visible daughters of each top squark, and $\vec{q}^{(i)}_{\text{T}}$ and $m_{\tilde{\chi}^0_1}$ are the transverse momentum and mass of the invisible $\tilde{\chi}^0_1$ from each top squark decay. The transverse mass, m^2_{T}, is

$$m^2_{\text{T}}(\vec{p}_{\text{T}}; m_{\text{p}}, \vec{q}_{\text{T}}; m_{\tilde{\chi}^0_1}) \equiv m^2_{\text{p}} + m^2_{\tilde{\chi}^0_1} + 2(E^p_{\text{T}} E^q_{\text{T}} - \vec{p}_{\text{T}} \cdot \vec{q}_{\text{T}}) \,. \tag{9}$$

M_{T2} is a minimization of two transverse masses with a constraint that the sum of the transverse momenta of both $\tilde{\chi}^0_1$'s is equal to the missing transverse momentum of the event, i.e., $\vec{q}^{(1)}_{\text{T}} + \vec{q}^{(2)}_{\text{T}} = \vec{p}^{\,\text{miss}}_{\text{T}}$. M_{T2} has a kinematic upper limit which is the $\tilde{\text{t}}$ mass. The invisible particle is assumed to be massless, therefore, $m_{\tilde{\chi}^0_1}$ equals zero in Eqs. 8–9.

We construct the visible portions of each $\tilde{\text{t}}$ particle ((1) and (2)) from the list of top-tagged objects. The baseline selection requirements ensure that every event has at least one reconstructed top-tagged object. In the case where two top-tagged objects are identified, each is used as one visible component in the M_{T2} calculation. If more than two top-tagged objects are found, M_{T2} is calculated for all combinations and the lowest M_{T2} value is taken. In the case where only one top-tagged object is identified, the visible component of the second system is taken from the remaining jets not included in the top-tagged object using a b-tagged jet as a seed to reconstruct a partial top quark. The b-tagged jet is combined with the closest jet which yields an

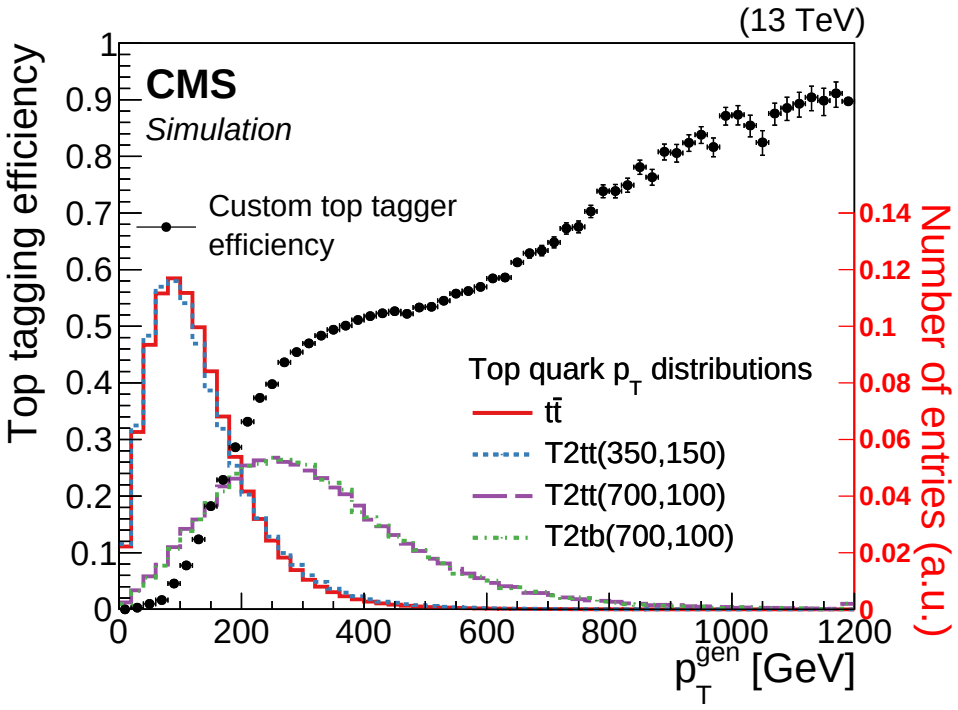

Figure 8: The tagging efficiency of the custom inclusive top tagger as a function of the generator-level hadronically decaying top quark p_T (black points). The error bar depicts the statistical uncertainty. The colored lines show the expected hadronically decaying top quark p_T distribution from $t\bar{t}$ (red), the T2tt signal model with $m_{\tilde{t}} = 350\,\text{GeV}$ and $m_{\tilde{\chi}_1^0} = 150\,\text{GeV}$ (blue), $m_{\tilde{t}} = 600\,\text{GeV}$ and $m_{\tilde{\chi}_1^0} = 200\,\text{GeV}$ (green), and $m_{\tilde{t}} = 700\,\text{GeV}$ and $m_{\tilde{\chi}_1^0} = 1\,\text{GeV}$ (purple). The top quark p_T distributions are normalized to unit area.

invariant mass between 50 GeV and the top quark mass. The combined "dijet" is used for the second visible system. In case no jet combination satisfies that invariant mass requirement, the b-tagged jet is used as the only remnant of the second visible system.

4.2 Event selection and categorization

Events in the search regions are collected with a Level-1 hardware trigger which requires that there be at least 175 GeV of calorimeter-based H_T in the event. If the event is accepted, the high-level trigger then requires a calorimeter-based $H_T > 280\,\text{GeV}$ and a calorimeter-based $\not{E}_T > 70\,\text{GeV}$. Finally, the high-level trigger applies a lower threshold of 350 GeV on the H_T over all PF-based jets in the event in coincidence with a threshold on the $\not{E}_T$ above 100 GeV computed using all PF candidates in the event. This analysis is fully efficient if one requires at least 175 GeV of PF-based $\not{E}_T$ together with at least 500 GeV of PF-based H_T.

This search targets multijet events, with b jets from top quark decays, large $\not{E}_T$ and no leptons. Initially, a loose pre-selection is applied, preserving 2-20% of the signal events. The pre-selection is defined using following criteria. All events must pass filters designed to remove detector- and beam-related noise. All jets considered in this analysis are required to have $p_T > 30\,\text{GeV}$, and must pass a set of "loose" jet identification criteria. The minimum number of such jets with $|\eta| < 2.4$ in an event must be $N_j \geq 4$, with the leading two jets required to have $p_T > 50\,\text{GeV}$. The missing transverse momentum must satisfy $\not{E}_T \geq 200\,\text{GeV}$, where the threshold is chosen to be past the trigger efficiency turn-on and to allow a low 175 GeV $< \not{E}_T$ sideband

for background studies. The scalar sum of jet p_T's must satisfy $H_T \geq 500\,\text{GeV}$, also chosen to be on the trigger efficiency plateau. Jets in the H_T calculation must meet the same jet selection criteria defined above. A requirement on the angle between $\not{E}_T$ and the first three leading jets, $\Delta\phi(\not{E}_T, j_{1,2,3}) > 0.5, 0.5, 0.3$, is applied to remove events from QCD multijet processes. Finally, requirements that $N_t \geq 1$, $N_b \geq 1$, and $M_{T2} > 200\,\text{GeV}$ are applied.

We bin the search regions in terms of the number of b-tagged jets and top-tagged objects, $\not{E}_T$, and M_{T2}. Figure 9 demonstrates the background composition following the pre-selection cuts as a function of N_t, N_b, $\not{E}_T$ and M_{T2}. Note that the top-tagged object definition does not require the presence of b-tagged jets, nor are b-tagged jets inside top-tagged objects rejected from the b-tagged jet counting. Thus there is not a one-to-one correspondence between the number of top-tagged objects and the number of b-tagged jets in an event. The number of b-tagged jets and top-tagged objects variables are binned as $N_b = 1$, $N_b \geq 2$ and $N_t = 1$, $N_t \geq 2$. To improve background suppression, in particular of the $t\bar{t}$ contribution, each (N_b,N_t) bin is further subdivided by placing requirements on the $\not{E}_T$ and M_{T2} variables. A total of 37 exclusive search bins are defined and illustrated in Fig. 10. The numbers displayed in the figure are the binning indices which are used throughout the analysis.

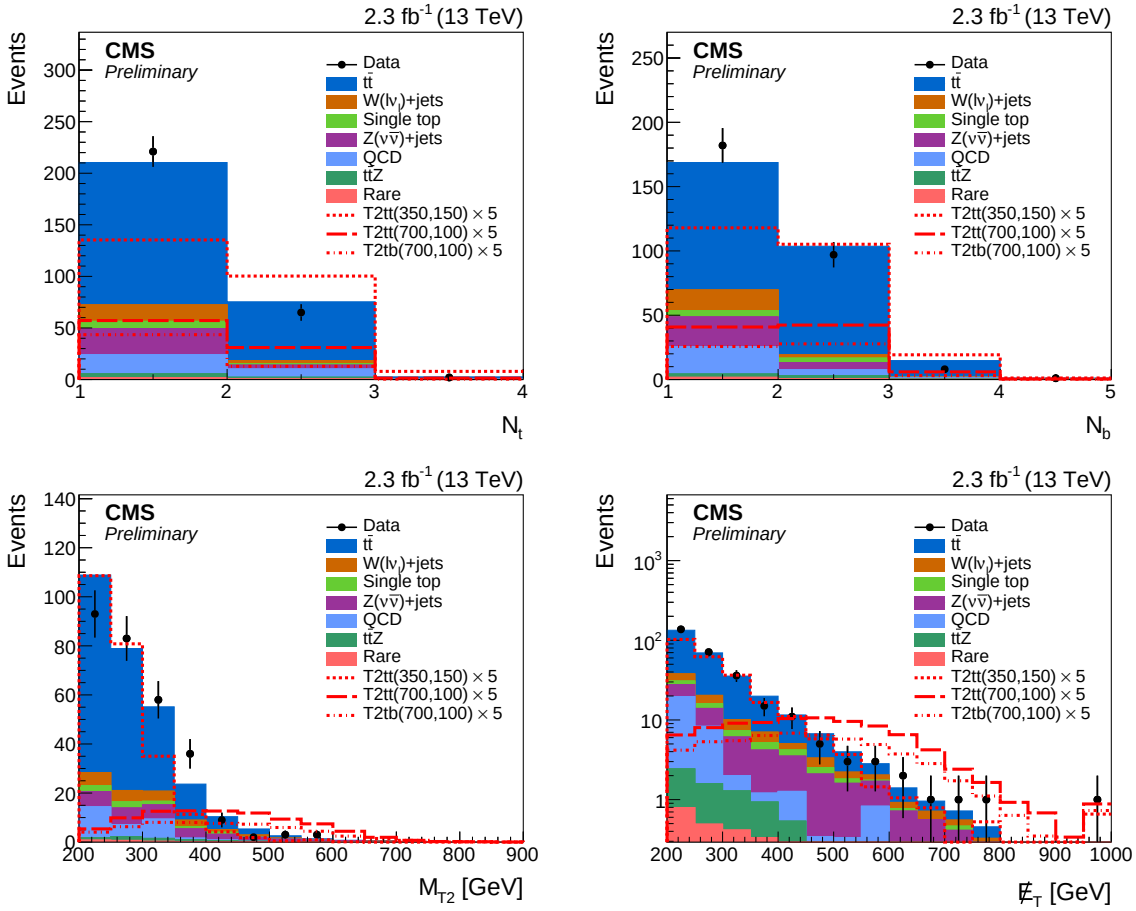

Figure 9: Comparison of the simulated distributions for N_t, N_b, $\not{E}_T$ and M_{T2} (clock-wise) between SM backgrounds (filled histograms) and several example T2tt signal models (dashed lines).

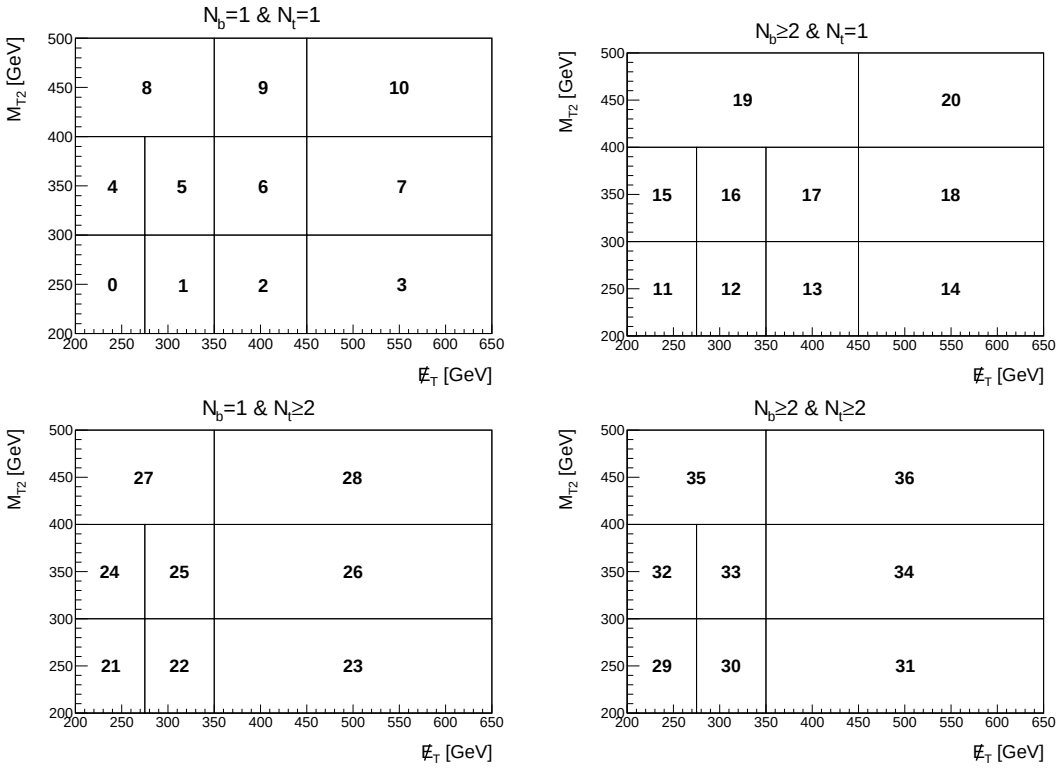

Figure 10: HETT search bin definitions after pre-selection cuts defined in the text. The highest $\not{E}_T$ and M_{T2} bins are open-ended, e.g., bin 10 requires $\not{E}_T > 450\,\text{GeV}$ and $M_{T2} > 400\,\text{GeV}$.

4.3 Estimation of the lost-lepton background

About 70% of the expected SM background (integrated over all search bins) comes from $t\bar{t}$ and W+jets events with leptonic W decays where one or more lepton is "lost". A lepton can be lost when electrons or muons are not isolated, not identified/reconstructed, or are out of the acceptance region. The lepton veto does not succeed in rejecting these events and they form an important background source for this analysis.

These lost leptons are modeled using appropriately weighted data events from a control sample which consists mainly of $t\bar{t}$ events. This control sample is defined to match the pre-selection, but the muon veto is replaced by the requirement that there be exactly one well identified and isolated muon and the isolated track veto is removed. To reduce possible signal contamination in this control sample, only events with a transverse mass less than 100 GeV are considered, with M_T reconstructed from the muon p_T and the event missing transverse energy as $M_T = \sqrt{2p_T^{\mu}E_T^{\text{miss}}(1-\cos(\Delta\phi))}$, where $\Delta\phi$ is the distance in ϕ between the muon and the $\not{E}_T$. For $t\bar{t}$ and W+jets events with one $W \to \mu\nu$ decay, $\not{E}_T$ originates from the produced neutrino. This means that the M_T distribution represents the transverse W-mass and falls off sharply above 80 GeV; however this is not the case for signal events.

The predicted number of $t\bar{t}$, W+jets and single top events with lost leptons, N_{LL} contributing to the search region is calculated as

$$N_{LL} = \sum_{CS}(F_{ISO} + F_{ID} + F_{Acc} \times F_{dilepton}) \times \frac{\epsilon_{isotrack}}{\epsilon^{\mu}_{M_T}}, \tag{10}$$

where $\sum_{CS}$ is the sum over the events measured directly in the single muon control sample de-

fined above. The factors F_{ISO}, F_{ID} and F_{Acc} convert the number of events in the control sample to the number of lost lepton events due to isolation, reconstruction or acceptance criteria, respectively. These scale factors are determined from isolation and reconstruction efficiencies, as well as the acceptance, which are obtained for each search region bin using simulated $\mathrm{t\bar{t}}$ events. The dilepton contribution is accounted for by the term F_{dilepton}. The control sample is normalized by the factor $\epsilon^{\mu}_{M_{\mathrm{T}}}$ to compensate for the efficiency of the $M_{\mathrm{T}} < 100\,\mathrm{GeV}$ requirement. Finally, the isolated track veto efficiency factor, $\epsilon_{\mathrm{isotrack}}$, is applied to get the final number of predicted lost lepton background events.

Dilepton events may contribute to the background in the signal region if both leptons are lost. In the muon control sample, dilepton events contribute when one lepton (electron or muon) is lost while the other one is reconstructed and identified as a muon. This effect is evaluated in simulated $\mathrm{t\bar{t}}$ events as the ratio between the number of events with one or two lost leptons over the number of events with one lost lepton plus twice the number of events with two lost leptons. A correction factor of $F^{\mu}_{\mathrm{dilepton}} = 99.3 \pm 0.02$ for muons and $F^{e}_{\mathrm{dilepton}} = 96.9 \pm 0.02$ for electrons.

The following sources of systematic uncertainty are included for the lost-lepton background prediction: lepton isolation efficiency, lepton reconstruction/ID efficiency, lepton acceptance from uncertainty in the PDFs, control sample purity, corrections due to the presence of dileptons, efficiency of the M_T selection cut, and isolated-track veto. In addition, a closure test is performed comparing the LL background in the search regions as predicted by applying the LL background determination procedure to the simulated muon control sample to the expectation obtained directly from $\mathrm{t\bar{t}}$, single top quark, and W+jets simulation. The result of the closure test is shown on the top plot of Fig. 11. A closure uncertainty of up to 26% is included as a systematic uncertainty in the LL background prediction.

4.4 Estimation of the hadronic tau background

Events from $\mathrm{t\bar{t}}$, $\mathrm{W}+\mathrm{jets}$ and single-top processes in which a τ lepton decays hadronically are one of the largest components of the SM background contributing to the search regions. When a W boson decays to a neutrino and a hadronically-decaying τ lepton (τ_{h}), the presence of neutrinos in the final state results in $\vec{p}_{\mathrm{T}}^{\,\mathrm{miss}}$, and the event passes the lepton veto because the hadronically-decaying τ is reconstructed as a jet. A veto on isolated tracks is used in the preselection to reduce the τ_{h} background while sustaining a minimal impact on signal efficiency. The remaining contribution from τ_{h} events in the signal regions, after applying this veto, is predicted using the method described below.

The estimate of this background is based on a control sample of $\mu+\mathrm{jets}$ events selected from data using a μ and H_{T}-based trigger, and requiring exactly one muon with $p^{\mu}_{\mathrm{T}} > 20\,\mathrm{GeV}$ and $|\eta| < 2.4$. A cut on the transverse mass of the W boson, $M_{\mathrm{T}} < 100\,\mathrm{GeV}$, is required to select events containing a $\mathrm{W} \to \mu\nu$ decay and to suppress signal events present in the $\mu+\mathrm{jets}$ sample. Because the $\mu+\mathrm{jets}$ and $\tau_{\mathrm{h}}+\mathrm{jets}$ events arise from the same physics processes, the hadronic component of the two samples is the same. The muon p_{T} is smeared by response template distributions derived for a hadronically-decaying τ lepton to correct the leptonic part of the event. The response templates are derived using $\mathrm{t\bar{t}}$ and $\mathrm{W}+\mathrm{jets}$ MC by comparing the true τ lepton p_{T} with the reconstructed τ_{h} jet p_{T}. The kinematic variables of the event are recalculated with this τ_{h} jet, and the search selections are applied to predict the τ_{h} background.

The probability to mistag a τ_{h} jet as a b jet is significant and must be taken into account in order to accurately predict the N_{b} distribution of τ_{h} background events. The dependence of the b-mistag rate on the τ_{h} jet p_{T} is larger for $\mathrm{t\bar{t}}$ events than for $\mathrm{W}+\mathrm{jets}$ events, because top

quark decays can cause overlap between the τ_h jet and the nearby b quark. This mistag rate is taken into account in the μ+jets control sample by randomly selecting a simulated τ_h jet and counting it as a b jet with the probability obtained from MC simulation in W + jets events for the corresponding τ_h jet p_T.

The veto of isolated tracks in the baseline selection helps to reject hadronically-decaying τ leptons, mostly one-prong taus. However, it also vetoes events containing isolated muons or electrons. Thus the veto cannot be directly applied to the μ+jets control sample. Instead, the isolated track veto efficiency ($\epsilon_{\text{isotrack}}$) for τ_h is determined from simulated $t\bar{t}$, W + jets and single-top events by matching isolated tracks to τ_h jets and computing the ratio of the number of tracks passing the isolation criteria over the total. The efficiency is applied as a correction factor to the μ+jets control sample yield.

The τ_h background prediction is calculated as follows:

$$N_{\tau_h} = \sum_{i}^{N_{\text{CS}}^{\mu}} \left(\sum_{j}^{\text{Template bins}} P_{\tau_h}^{\text{resp}} \frac{\epsilon_{\tau\to\mu}}{\epsilon_{\text{trigger}}^{\mu}\,\epsilon_{\text{reco}}^{\mu}\,\epsilon_{\text{iso}}^{\mu}\,\epsilon_{\text{acc}}^{\mu}\,\epsilon_{M_T}^{\mu}} \frac{\mathcal{B}(W\to\tau_h)}{\mathcal{B}(W\to\mu)}\,\epsilon_{\text{isotrack}}\,F_{\text{dilepton}} \right) \tag{11}$$

where the first summation is over the events in the μ + jets control sample, the second is over the bins of the τ_h response template and $P_{\tau_h}^{\text{resp}}$ is the probability of τ_h response from each bin. The various correction factors applied to convert μ + jets events into τ_h + jets events to construct the final τ_h sample are the branching ratio $\mathcal{B}(W \to \tau_h)/\mathcal{B}(W \to \mu) = 0.65$; the muon reconstruction and identification efficiency $\epsilon_{\text{reco}}^{\mu}$ and the muon isolation efficiency $\epsilon_{\text{iso}}^{\mu}$; the muon kinematic and geometric acceptance $\epsilon_{\text{acc}}^{\mu}$; the M_T selection efficiency ϵ_{M_T}; the contamination in the control sample from muons from τ decays, $\epsilon_{\tau\to\mu}$; the isolated track veto efficiency for τ_h, $\epsilon_{\text{isotrack}}$; the τ_h contribution that overlaps with the lost-lepton prediction due to contamination of dileptonic events in the control sample, F_{dilepton}, that would result in double counting; and a correction for the μ trigger efficiency, $\epsilon_{\text{trigger}}^{\mu}$. The muon reconstruction, identification, and isolation efficiency are the same as used for the lost-lepton background determination.

Systematic uncertainties are evaluated for each of the ingredients in the prediction, which arise from the following sources: uncertainties in the hadronic tau response template, uncertainties in the muon reconstruction and isolation efficiency, uncertainties in the acceptance due to uncertainties in the PDFs, uncertainties in the b-mistag rate of the τ_h jet, uncertainties in ϵ_{M_T} due to uncertainties in the $\not{E}_T$ scale, uncertainties in the efficiency of the isolated track veto, uncertainties due to contamination from lost leptons, uncertainties in the trigger efficiency. Additionally, a closure test is performed comparing the τ_h background in the search regions as predicted by applying the τ_h background determination procedure to the simulated muon control sample to the expectation obtained directly from $t\bar{t}$, single top quark, and W+jets simulation. The result of the closure test is shown in the lower plot of Fig. 11. A closure uncertainty of up to 28% is included as a systematic uncertainty in the τ_h background prediction.

4.5 Estimation of the $Z \to \nu\nu$ background

The $Z \to \nu\nu$ background is derived using simulated events that have been corrected for observed differences between data and simulation for both shape and normalization. The comparisons are made in a dimuon control region, exploiting the correspondence between $Z \to \nu\nu$ and $Z \to \mu\mu$ events. A loose set of selection criteria are used to make shape estimates based on N_j. The normalization correction is derived in a tighter control region closely matching the analysis pre-selection, which lacks the statistical precision for a full shape comparison.

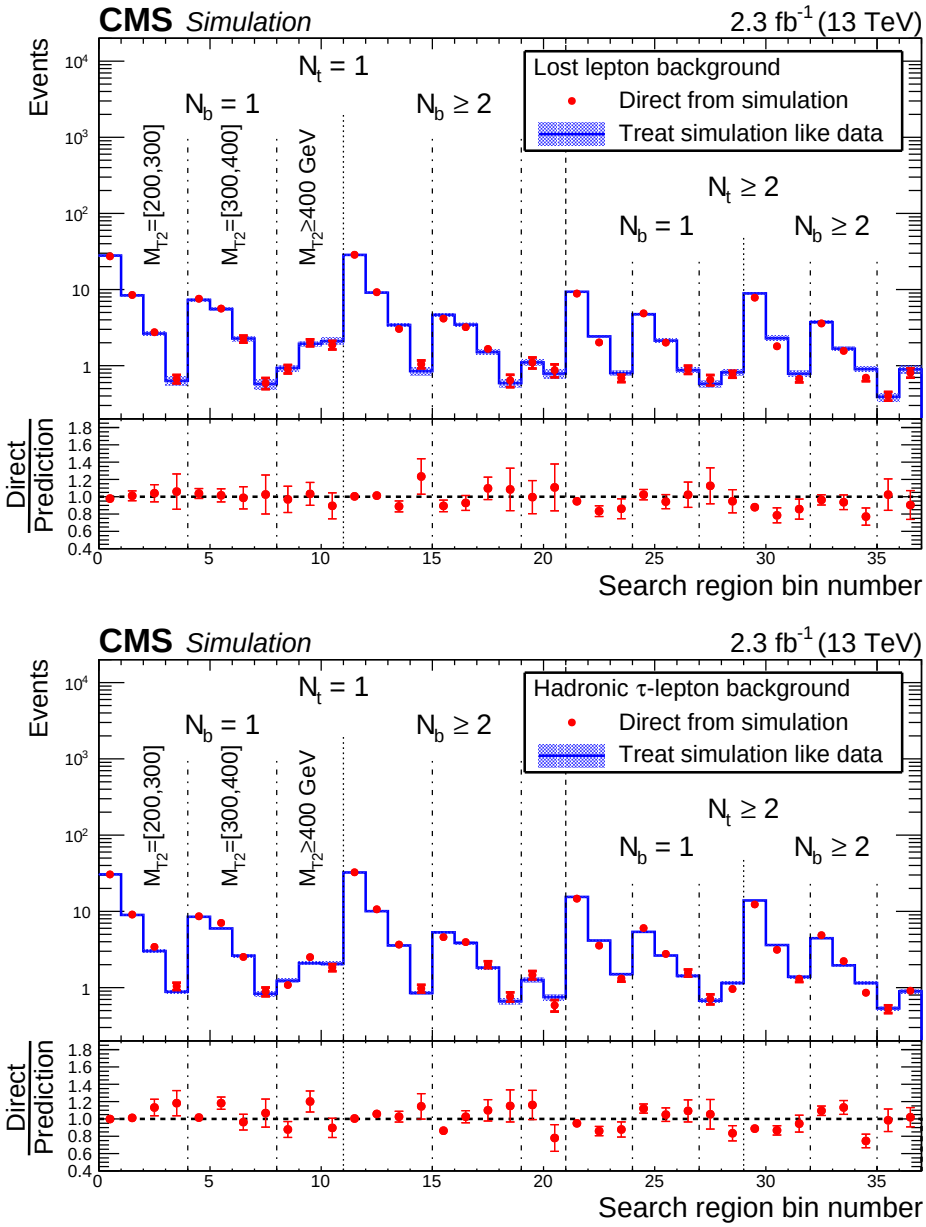

Figure 11: (upper plot) The lost-lepton background in the 37 search regions of the analysis as determined directly from $t\bar{t}$, single top quark, and W+jets simulation (points) and as predicted by applying the lost-lepton background determination procedure to the simulated muon control sample (histograms). The lower panel shows the same results following division by the predicted value. Only statistical uncertainties are shown. (lower plot) The corresponding simulated results for the background from hadronically-decaying τ leptons. For both plots, vertical lines indicate search regions with different N_t, N_b, and M_{T2} values, as defined in Fig. 10.

The central value of the $Z \to \nu\nu$ background prediction for each search bin B can be written as

$$\widehat{N}_B = R_{\text{norm}} \cdot \sum_{\text{events} \in B} S_{\text{DY}}(N_{\text{j}}) w_{\text{MC}}, \tag{12}$$

where $\widehat{N}_B$ is the predicted number of $Z \to \nu\nu$ background events in search bin B and w_{MC} is a standard MC event weight including the assumed $Z \to \nu\nu$ cross section, the data luminosity, the b-tagging efficiency scale factors and the measured trigger efficiency. Each simulated event is weighted using two scale factors, R_{norm} and $S_{\text{DY}}(N_{\text{j}})$, that correct the normalization and the shape of the simulation, respectively. Both scale factors are calculated in a dimuon control region including events with two muons, with $81 < m_{\mu\mu} < 101\,\text{GeV}$, and no muon or isolated track vetos. In this region the two muons are treated as if they were neutrinos.

The first scale factor, R_{norm}, is an overall normalization factor for the $Z \to \nu\nu$ simulation that is derived in a tight dimuon control region in data. This tight dimuon control region has the same selection as the search region pre-selection, apart from the muon requirement and without any requirements on b-tagged jets. This region is selected for its kinematic similarity to the signal region, but lacks the statistical precision required for shape comparison. The scale factor is computed by comparing the expected event yield in the tight region in the Drell-Yan (DY) simulation with the observed event yield in data after subtraction of the other SM processes.

The second scale factor, S_{DY}, depends on the number of jets (N_{j}) in the event and is designed to correct the mismodeling of the jet multiplicity distribution in simulation. The scale factor is derived in a loose dimuon control region in which the signal region requirements on $\not{E}_{\text{T}}$, N_{t} and M_{T2} are removed, and the H_{T} requirement is relaxed to $H_{\text{T}} > 200\,\text{GeV}$. This region provides a data sample that is close to the signal region in terms of kinematic requirements, e.g. the number of jets, but is also loose enough to have sufficient events to do a shape comparison for the main analysis variables. The S_{DY} scale factor is derived for each (N_{j}) bin as the ratio between the data, with non-DY backgrounds subtracted, and the DY MC. Due to $\text{t}\bar{\text{t}}$ contributions similar to the DY processes for larger jet and b-tagged jet multiplicities, the $\text{t}\bar{\text{t}}$ MC is similarly reweighted using a control region selected to have an electron and a muon with $81 < m_{e\mu} < 101\,\text{GeV}$ before subtraction from the dimuon data. The N_{b} and $\not{E}_{\text{T}}$ distributions in the loose control region after applying the $S_{DY}(N_{\text{j}})$ scale factor are shown in Fig. 12. The N_{b} distribution agrees very well between data and simulation, whereas some discrepancies remain for the $\not{E}_{\text{T}}$ distribution.

The systematic uncertainties for the $Z \to \nu\nu$ background prediction can be divided in two broad categories: uncertainties associated with the use of MC simulation and uncertainties specifically associated with the background prediction method. The first category includes systematic uncertainties on PDF and renormalization/factorization scale choices, jet and $\not{E}_{\text{T}}$ energy scale uncertainties, b-tag scale factor uncertainties and trigger efficiency uncertainties. The second category includes uncertainties from the method used to determine R_{norm} and the $S_{DY}(N_{\text{j}})$ scale factors, and uncertainties based on the residual shape disagreement between data and DY MC in the loose dimuon control region. The uncertainty in R_{norm} results in a 19.4% uncertainty in the predicted $Z \to \nu\nu$ event yield for each search bin. The uncertainties associated with S_{DY} are the dominant uncertainties and are related to residual shape uncertainties (after applying the S_{DY} scale factor) in the search region variables $\not{E}_{\text{T}}$, M_{T2}, N_{b} and N_{t}. These uncertainties are evaluated in the loose control region with the additional requirement that $N_{\text{t}} \geq 1$ so that M_{T2} is well-defined. Comparisons between data and simulation for each considered variable are made and any observed differences are propagated to the prediction of the event yields for each signal bin. The resulting shift of the central value of the search bin predictions is used as the systematic uncertainty from residual shape disagreements. Depend-

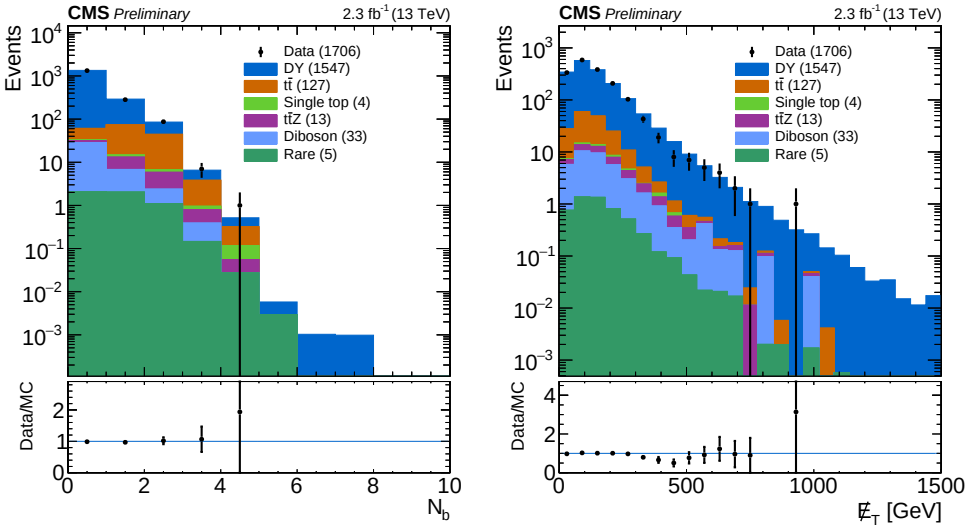

Figure 12: N_{b} (left) and $\not{E}_{\mathrm{T}}$ (right) distribution in data and simulation in the loose control region after applying the $S_{DY}(N_{\mathrm{j}})$ scale factor to the simulation. The lower panels show the ratio between data and simulation. Only statistical uncertainties are shown.

ing on the search bin, this uncertainty ranges between 10 and 82%. The statistical uncertainties in the ratios between data and simulation, as well as in S_{DY}, are also included as a 15–75% systematic uncertainty in the prediction.

4.6 Estimation of the QCD multijet background

One of the challenging consequences of the strong reduction of the QCD multijet contribution in the signal region when applying the selection criteria is that the QCD multijet contribution is also very small in control regions that are kinematically close to the signal region. Furthermore, these control regions are frequently dominated by $\mathrm{t\bar{t}}$ processes, making it difficult to directly extract a QCD multijet prediction for the signal region using the control regions. The procedure adopted here consists in selecting a signal-depleted data control sample, rich in QCD multijet events, from which significant contributions of other SM backgrounds, such as $\mathrm{t\bar{t}}$, W+jets, and Z+jets, are subtracted. Following that, a translation factor, partly determined by data and partly by simulation, is used to convert the number of QCD multijet events measured in the data control region into a QCD multijet prediction for each search region bin.

The signal-depleted, QCD multijet-enriched control sample is defined by applying the full set of pre-selection cuts, described in Sec. 4.2, except that the $\Delta\phi(\not{E}_{\mathrm{T}}, j_{1,2,3})$ requirements are inverted. High-$\not{E}_{\mathrm{T}}$ QCD multijet events are usually the result of an undermeasurement of the p_{T} of one of the leading jets, which results in $\not{E}_{\mathrm{T}}$ being aligned with that jet and $\Delta\phi(\not{E}_{\mathrm{T}}, j_{1,2,3})$ being small.

The estimated number of QCD multijet events in the inverted-$\Delta\phi$ region is computed by subtracting the contributions from lost leptons, hadronic τ's, and Z+jets processes from the number of data events observed in that region,

$$N_{\mathrm{QCD}}^{\mathrm{CR}} = N_{\mathrm{Data}}^{\mathrm{CR}} - N_{\mathrm{LL}}^{\mathrm{CR}} - N_{\tau_{\mathrm{h}}}^{\mathrm{CR}} - N_{\mathrm{Z}\to\nu\nu}^{\mathrm{CR}} \,. \tag{13}$$

The same methods as described in the previous sections are used to estimate $N_{\mathrm{LL}}^{\mathrm{CR}}$ and $N_{\tau_{\mathrm{h}}}^{\mathrm{CR}}$, but applied to this QCD multijet-enriched control region. Simulation is used to estimate $N_{\mathrm{Z}\to\nu\nu}^{\mathrm{CR}}$ since the contribution is expected to be small.

The translation factor between the QCD multijet-enriched control region and the search region bins may depend on some of the kinematic observables used to define the search bins. However, since the translation factor is a ratio, any such dependence is expected to be mild. Because of the small size of the data control sample in the high-$\not\!\!E_T$ regions, the value of the translation factor is constrained to a data measurement in a sideband of the pre-selection region, defined by the requirement $175 < \not\!\!E_T < 200\,\text{GeV}$, where the amount of data is sufficiently large to make an accurate measurement. Any possible kinematic dependence on $\not\!\!E_T$ or M_{T2} is accounted for by using a linear approximation derived from simulation. Its slope in $\not\!\!E_T$ and M_{T2} is taken from simulation and its offset is fixed by the data measurement in the low $\not\!\!E_T$ sideband. The translation factor, T_{QCD}, scales the number of QCD multijet events measured in the QCD multijet-enriched control region into a QCD multijet-prediction for a given search region bin:

$$N_{QCD}^{SR} = T_{QCD} \times N_{QCD}^{CR} \,. \tag{14}$$

A closure test is performed in simulation to assess how well the method works. In this closure test the expectation for the signal region event yields as obtained directly from the QCD multijet simulation is compared to the prediction obtained by applying the QCD multijet background determination procedure to simulated event samples. The result of this test is shown in Fig. 13, and any observed non-closure is taken into account as a systematic uncertainty in the QCD multijet prediction. The dominant sources of systematic uncertainty in the QCD multijet prediction are the uncertainties in the T_{QCD} factors, uncertainties from the closure test, and the trigger efficiency.

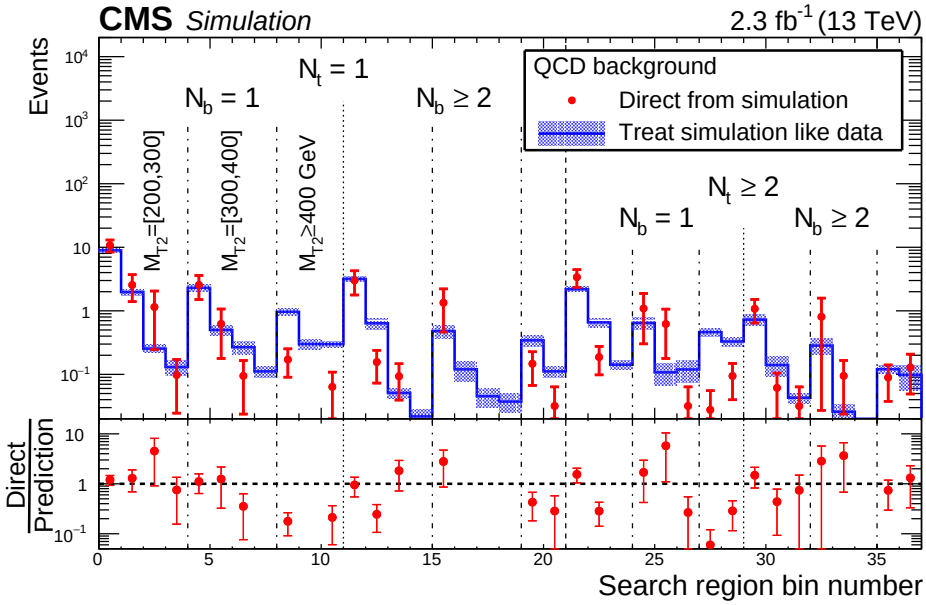

Figure 13: The QCD multijet background in the 37 search regions of the analysis as determined directly from QCD multijet simulation (points) and as predicted by applying the QCD multijet background determination procedure to simulated event samples (histograms). The lower panel shows the same results following division by the predicted value. Only statistical uncertainties are shown. The labeling of the search regions is the same as in Fig. 11.

4.7 Results

The predicted number of SM background events and the number of events observed in data for each of the search regions defined in Section 4.2 are summarized in Figure 14 and Table 4.

Typically, the most significant background across the search regions comes from the SM $t\bar{t}$ production or W-boson production, where either $W \to \ell\nu$ and the lepton ($\ell = e, \mu$) is not detected or $W \to \tau\nu$ and the τ lepton decays hadronically. Generally, the next largest contribution comes from $Z \to \nu\nu$ production in association with jets (including heavy-flavor jets) in which the neutrino pair gives large $\not{E}_T$ and the top quark conditions are satisfied by an accidental combination of the jets. The QCD multijet contribution and the contribution from other rare SM processes are sub-dominant across all bins. The largest rare SM process contribution (though still small) comes from $t\bar{t}Z$ with the Z boson decaying into a pair of neutrinos. This background is estimated in an identical way to that described in Section 3.5.

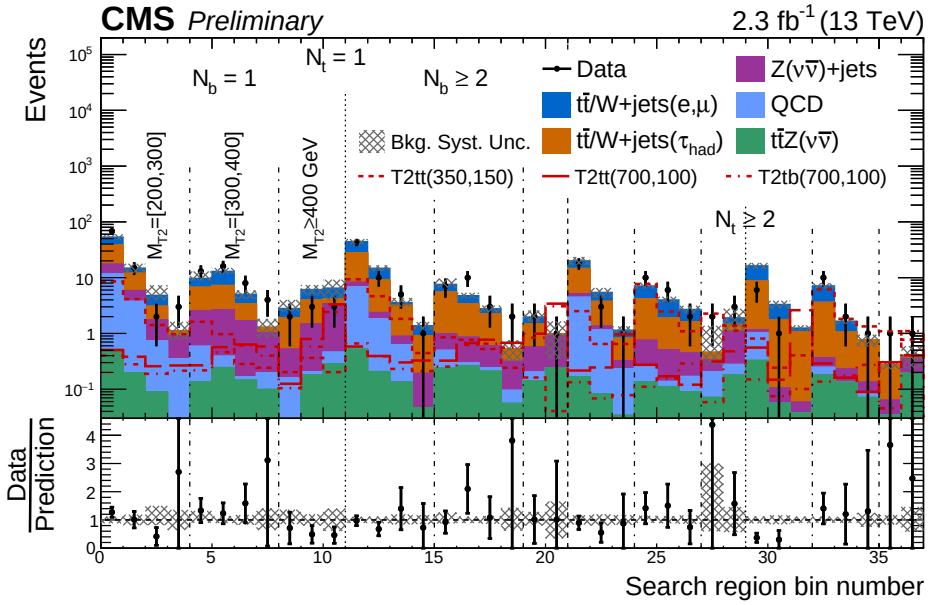

Figure 14: Observed event yields in data (black points) and predicted SM background (filled solid area) for the 37 search bins of the HETT analysis. The bottom plot shows the ratio of data over total background prediction in each search bin. Only statistical uncertainties are propagated to the ratio.

5 Interpretation

The statistical interpretation of the results in terms of exclusion limits for the signal models considered is based on a binned likelihood fit to the observed data, taking into account the predicted background and expected signal yields with their uncertainties in each bin. The extraction of exclusion limits is based on a modified frequentist approach [63] using a profile likelihood ratio as test statistic. Signal models for which the 95% upper limit on the production cross section falls below the theoretical cross section (based on NLO+NLL calculations [55]) are considered to be excluded by the analysis.

The uncertainties in the signal modeling are determined per search region bin and include the following sources: simulation sample size (up to 100%), luminosity determination (2.7%), lepton and isolated track veto (up to 6%), b tag efficiency corrections used to scale simulation to data (up to 36%), trigger efficiency ($< 1\%$), QCD renormalization and factorization scales (up to 3%), initial-state radiation (up to 30%), jet energy scale corrections (up to 47%), and the modeling of the fast-simulation compared with the full-simulation for top quark reconstruction

Table 4: Observed yields from the data compared to the total background predictions for the search bins of the HETT analysis. Uncertainties are listed ± stat. ± syst.

$\not{E}_T$ [GeV]	Data	Total SM	Lost lepton	Had. τ	$Z \to \nu\nu$	QCD	$t\bar{t}Z$
$N_t = 1,\ N_b = 1,\ 200 \le M_{T2} < 300$ GeV							
200 – 275	68	$54^{+4}_{-4}{}^{+6}_{-6}$	$15^{+3}_{-3}{}^{+2}_{-2}$	$21^{+2}_{-2}{}^{+1}_{-1}$	$5.74^{+0.09}_{-0.09}{}^{+1.56}_{-1.56}$	$11^{+1}_{-1}{}^{+6}_{-6}$	$0.51^{+0.04}_{-0.04}{}^{+0.18}_{-0.18}$
275 – 350	15	$15^{+2}_{-2}{}^{+3}_{-3}$	$2.8^{+1.6}_{-1.2}{}^{+0.4}_{-0.4}$	$6.2^{+1.3}_{-1.2}{}^{+0.5}_{-0.5}$	$2.11^{+0.05}_{-0.05}{}^{+0.67}_{-0.67}$	$3.6^{+0.8}_{-0.8}{}^{+2.7}_{-2.7}$	$0.20^{+0.02}_{-0.02}{}^{+0.07}_{-0.07}$
350 – 450	2	$4.9^{+1.6}_{-1.2}{}^{+2.4}_{-0.9}$	$1.8^{+1.5}_{-1.1}{}^{+0.3}_{-0.3}$	$1.3^{+0.6}_{-0.3}{}^{+0.2}_{-0.2}$	$1.01^{+0.03}_{-0.03}{}^{+0.53}_{-0.53}$	$0.6^{+0.3}_{-0.3}{}^{+2.4}_{-0.6}$	$0.09^{+0.02}_{-0.02}{}^{+0.03}_{-0.03}$
450+	3	$1.2^{+1.1}_{-0.2}{}^{+0.4}_{-0.4}$	$0.00^{+0.88}_{-0.00}{}^{+0.00}_{-0.00}$	$0.22^{+0.56}_{-0.09}{}^{+0.03}_{-0.04}$	$0.54^{+0.02}_{-0.02}{}^{+0.29}_{-0.29}$	$0.3^{+0.2}_{-0.2}{}^{+0.3}_{-0.3}$	$0.01^{+0.00}_{-0.00}{}^{+0.00}_{-0.01}$
$N_t = 1,\ N_b = 1,\ 300 \le M_{T2} < 400$ GeV							
200 – 275	13	$9.8^{+1.8}_{-1.5}{}^{+3.1}_{-1.0}$	$3.0^{+1.5}_{-1.2}{}^{+0.5}_{-0.5}$	$4.2^{+1.1}_{-1.0}{}^{+0.3}_{-0.3}$	$1.96^{+0.05}_{-0.05}{}^{+0.63}_{-0.63}$	$0.45^{+0.09}_{-0.09}{}^{+3.00}_{-0.45}$	$0.14^{+0.02}_{-0.02}{}^{+0.04}_{-0.04}$
275 – 350	16	$13^{+2}_{-2}{}^{+2}_{-1}$	$5.8^{+2.1}_{-1.8}{}^{+0.9}_{-0.9}$	$4.6^{+1.2}_{-1.1}{}^{+0.7}_{-0.7}$	$2.24^{+0.06}_{-0.06}{}^{+0.89}_{-0.89}$	$0.15^{+0.05}_{-0.05}{}^{+0.97}_{-0.15}$	$0.24^{+0.03}_{-0.03}{}^{+0.09}_{-0.09}$
350 – 450	8	$5.0^{+1.7}_{-1.1}{}^{+0.9}_{-0.9}$	$1.6^{+1.5}_{-1.0}{}^{+0.3}_{-0.3}$	$1.7^{+0.8}_{-0.5}{}^{+0.2}_{-0.2}$	$1.51^{+0.04}_{-0.04}{}^{+0.80}_{-0.80}$	$0.02^{+0.05}_{-0.05}{}^{+0.06}_{-0.02}$	$0.15^{+0.02}_{-0.02}{}^{+0.05}_{-0.05}$
450+	4	$1.3^{+1.1}_{-0.1}{}^{+0.5}_{-0.5}$	$0.00^{+0.91}_{-0.00}{}^{+0.00}_{-0.00}$	$0.25^{+0.56}_{-0.12}{}^{+0.04}_{-0.04}$	$0.84^{+0.03}_{-0.03}{}^{+0.45}_{-0.45}$	$0.10^{+0.07}_{-0.07}{}^{+0.28}_{-0.10}$	$0.10^{+0.02}_{-0.02}{}^{+0.04}_{-0.04}$
$N_t = 1,\ N_b = 1,\ M_{T2} > 400$ GeV							
200 – 350	2	$2.9^{+1.3}_{-0.8}{}^{+1.1}_{-0.4}$	$0.9^{+1.0}_{-0.5}{}^{+0.2}_{-0.2}$	$1.4^{+0.8}_{-0.6}{}^{+0.2}_{-0.2}$	$0.36^{+0.02}_{-0.02}{}^{+0.28}_{-0.28}$	$0.15^{+0.05}_{-0.05}{}^{+0.98}_{-0.15}$	$0.01^{+0.01}_{-0.01}{}^{+0.00}_{-0.00}$
350 – 450	3	$6^{+2}_{-2}{}^{+1}_{-1}$	$2.2^{+1.9}_{-1.3}{}^{+0.4}_{-0.4}$	$2.5^{+1.0}_{-0.9}{}^{+0.4}_{-0.4}$	$1.26^{+0.04}_{-0.04}{}^{+1.08}_{-1.08}$	$0.02^{+0.05}_{-0.05}{}^{+0.07}_{-0.02}$	$0.18^{+0.02}_{-0.02}{}^{+0.07}_{-0.06}$
450+	3	$7^{+2}_{-1}{}^{+3}_{-3}$	$2.3^{+2.0}_{-1.4}{}^{+0.5}_{-0.5}$	$0.8^{+0.7}_{-0.5}{}^{+0.1}_{-0.1}$	$2.93^{+0.06}_{-0.06}{}^{+2.53}_{-2.53}$	$0.18^{+0.10}_{-0.10}{}^{+0.52}_{-0.18}$	$0.28^{+0.03}_{-0.03}{}^{+0.10}_{-0.10}$
$N_t = 1,\ N_b \ge 2,\ 200 \le M_{T2} < 300$ GeV							
200 – 275	43	$44^{+4}_{-4}{}^{+5}_{-5}$	$16^{+3}_{-3}{}^{+2}_{-2}$	$20^{+2}_{-2}{}^{+1}_{-1}$	$1.38^{+0.04}_{-0.04}{}^{+0.96}_{-0.96}$	$6^{+1}_{-1}{}^{+4}_{-4}$	$0.52^{+0.04}_{-0.04}{}^{+0.17}_{-0.17}$
275 – 350	10	$15^{+3}_{-2}{}^{+2}_{-2}$	$5.7^{+2.1}_{-1.8}{}^{+0.9}_{-0.9}$	$6.7^{+1.5}_{-1.4}{}^{+0.5}_{-0.5}$	$0.53^{+0.03}_{-0.03}{}^{+0.39}_{-0.39}$	$1.6^{+0.6}_{-0.6}{}^{+1.4}_{-1.4}$	$0.21^{+0.03}_{-0.03}{}^{+0.07}_{-0.07}$
350 – 450	5	$3.6^{+1.5}_{-0.9}{}^{+0.7}_{-0.6}$	$0.39^{+1.20}_{-0.39}{}^{+0.07}_{-0.07}$	$2.3^{+0.9}_{-0.8}{}^{+0.2}_{-0.2}$	$0.26^{+0.02}_{-0.02}{}^{+0.21}_{-0.21}$	$0.5^{+0.3}_{-0.3}{}^{+0.6}_{-0.5}$	$0.14^{+0.02}_{-0.02}{}^{+0.05}_{-0.05}$
450+	1	$1.4^{+1.5}_{-0.7}{}^{+0.2}_{-0.2}$	$0.5^{+1.3}_{-0.5}{}^{+0.1}_{-0.1}$	$0.71^{+0.71}_{-0.44}{}^{+0.10}_{-0.10}$	$0.14^{+0.01}_{-0.01}{}^{+0.13}_{-0.13}$	$0.00^{+0.13}_{-0.13}{}^{+0.11}_{-0.00}$	$0.05^{+0.01}_{-0.01}{}^{+0.02}_{-0.02}$
$N_t = 1,\ N_b \ge 2,\ 300 \le M_{T2} < 400$ GeV							
200 – 275	7	$7.6^{+1.7}_{-1.4}{}^{+2.0}_{-0.9}$	$2.1^{+1.2}_{-0.8}{}^{+0.4}_{-0.4}$	$4.5^{+1.2}_{-1.1}{}^{+0.7}_{-0.7}$	$0.49^{+0.03}_{-0.03}{}^{+0.34}_{-0.34}$	$0.26^{+0.06}_{-0.06}{}^{+1.78}_{-0.26}$	$0.24^{+0.03}_{-0.03}{}^{+0.09}_{-0.09}$
275 – 350	10	$4.8^{+1.7}_{-1.1}{}^{+0.6}_{-0.5}$	$1.4^{+1.4}_{-0.8}{}^{+0.2}_{-0.2}$	$2.5^{+1.0}_{-0.8}{}^{+0.2}_{-0.2}$	$0.55^{+0.03}_{-0.03}{}^{+0.41}_{-0.41}$	$0.04^{+0.03}_{-0.03}{}^{+0.24}_{-0.04}$	$0.26^{+0.03}_{-0.03}{}^{+0.09}_{-0.09}$
350 – 450	3	$2.8^{+1.6}_{-0.9}{}^{+0.4}_{-0.4}$	$0.5^{+1.4}_{-0.5}{}^{+0.1}_{-0.1}$	$1.6^{+0.9}_{-0.7}{}^{+0.2}_{-0.2}$	$0.35^{+0.02}_{-0.02}{}^{+0.29}_{-0.29}$	$0.03^{+0.05}_{-0.05}{}^{+0.09}_{-0.03}$	$0.21^{+0.03}_{-0.03}{}^{+0.08}_{-0.07}$
450+	2	$0.5^{+1.3}_{-0.1}{}^{+0.2}_{-0.2}$	$0.00^{+1.13}_{-0.00}{}^{+0.00}_{-0.00}$	$0.21^{+0.57}_{-0.13}{}^{+0.03}_{-0.03}$	$0.22^{+0.01}_{-0.01}{}^{+0.19}_{-0.19}$	$0.04^{+0.05}_{-0.05}{}^{+0.11}_{-0.04}$	$0.06^{+0.01}_{-0.01}{}^{+0.02}_{-0.02}$
$N_t = 1,\ N_b \ge 2,\ M_{T2} > 400$ GeV							
200 – 450	2	$2.0^{+1.4}_{-0.7}{}^{+0.6}_{-0.4}$	$0.5^{+1.2}_{-0.5}{}^{+0.1}_{-0.1}$	$0.9^{+0.7}_{-0.5}{}^{+0.1}_{-0.1}$	$0.36^{+0.02}_{-0.02}{}^{+0.35}_{-0.35}$	$0.06^{+0.03}_{-0.03}{}^{+0.41}_{-0.06}$	$0.14^{+0.02}_{-0.02}{}^{+0.05}_{-0.05}$
450+	1	$0.99^{+1.77}_{-0.06}{}^{+0.65}_{-0.65}$	$0.00^{+1.68}_{-0.00}{}^{+0.00}_{-0.00}$	$0.09^{+0.55}_{-0.05}{}^{+0.02}_{-0.02}$	$0.66^{+0.02}_{-0.02}{}^{+0.65}_{-0.65}$	$0.00^{+0.07}_{-0.00}{}^{+0.00}_{-0.00}$	$0.24^{+0.03}_{-0.03}{}^{+0.09}_{-0.09}$
$N_t \ge 2,\ N_b = 1,\ 200 \le M_{T2} < 300$ GeV							
200 – 275	18	$20^{+2}_{-2}{}^{+3}_{-3}$	$5.4^{+1.7}_{-1.6}{}^{+1.0}_{-0.9}$	$9.5^{+1.5}_{-1.4}{}^{+0.9}_{-0.9}$	$0.67^{+0.03}_{-0.03}{}^{+0.48}_{-0.48}$	$4.3^{+0.9}_{-0.9}{}^{+3.0}_{-3.0}$	$0.17^{+0.02}_{-0.02}{}^{+0.05}_{-0.05}$
275 – 350	3	$5^{+1}_{-1}{}^{+1}_{-1}$	$1.7^{+0.9}_{-0.7}{}^{+0.4}_{-0.4}$	$2.4^{+0.9}_{-0.7}{}^{+0.4}_{-0.4}$	$0.20^{+0.01}_{-0.01}{}^{+0.15}_{-0.15}$	$1.1^{+0.4}_{-0.4}{}^{+0.9}_{-0.9}$	$0.08^{+0.02}_{-0.02}{}^{+0.03}_{-0.03}$
350+	1	$1.1^{+0.9}_{-0.5}{}^{+0.2}_{-0.2}$	$0.32^{+0.59}_{-0.32}{}^{+0.07}_{-0.07}$	$0.50^{+0.65}_{-0.34}{}^{+0.08}_{-0.08}$	$0.09^{+0.01}_{-0.01}{}^{+0.08}_{-0.08}$	$0.2^{+0.2}_{-0.2}{}^{+0.1}_{-0.1}$	$0.03^{+0.01}_{-0.01}{}^{+0.01}_{-0.01}$
$N_t \ge 2,\ N_b = 1,\ 300 \le M_{T2} < 400$ GeV							
200 – 275	10	$7.1^{+1.8}_{-1.5}{}^{+1.1}_{-0.7}$	$2.9^{+1.5}_{-1.3}{}^{+0.5}_{-0.5}$	$3.4^{+1.0}_{-0.9}{}^{+0.4}_{-0.4}$	$0.50^{+0.02}_{-0.02}{}^{+0.37}_{-0.37}$	$0.11^{+0.05}_{-0.05}{}^{+0.77}_{-0.11}$	$0.14^{+0.02}_{-0.02}{}^{+0.04}_{-0.04}$
275 – 350	6	$4.0^{+1.5}_{-1.1}{}^{+0.5}_{-0.5}$	$2.1^{+1.3}_{-1.0}{}^{+0.4}_{-0.4}$	$1.4^{+0.7}_{-0.4}{}^{+0.1}_{-0.1}$	$0.37^{+0.02}_{-0.02}{}^{+0.28}_{-0.28}$	$0.03^{+0.02}_{-0.02}{}^{+0.21}_{-0.03}$	$0.11^{+0.02}_{-0.02}{}^{+0.03}_{-0.04}$
350+	2	$2.7^{+1.2}_{-0.8}{}^{+0.4}_{-0.4}$	$1.1^{+0.9}_{-0.7}{}^{+0.2}_{-0.2}$	$1.2^{+0.7}_{-0.5}{}^{+0.2}_{-0.2}$	$0.28^{+0.02}_{-0.02}{}^{+0.23}_{-0.23}$	$0.08^{+0.07}_{-0.07}{}^{+0.23}_{-0.08}$	$0.09^{+0.02}_{-0.02}{}^{+0.03}_{-0.03}$
$N_t \ge 2,\ N_b = 1,\ M_{T2} > 400$ GeV							
200 – 250	2	$0.5^{+1.1}_{-0.1}{}^{+0.9}_{-0.2}$	$0.00^{+0.93}_{-0.00}{}^{+0.00}_{-0.00}$	$0.12^{+0.56}_{-0.12}{}^{+0.02}_{-0.02}$	$0.13^{+0.01}_{-0.01}{}^{+0.12}_{-0.12}$	$0.14^{+0.04}_{-0.04}{}^{+0.91}_{-0.14}$	$0.07^{+0.01}_{-0.01}{}^{+0.03}_{-0.03}$
350+	3	$1.9^{+1.1}_{-0.5}{}^{+0.9}_{-0.8}$	$0.45^{+0.93}_{-0.45}{}^{+0.09}_{-0.09}$	$0.36^{+0.59}_{-0.22}{}^{+0.07}_{-0.07}$	$0.81^{+0.03}_{-0.03}{}^{+0.82}_{-0.81}$	$0.10^{+0.09}_{-0.09}{}^{+0.28}_{-0.10}$	$0.18^{+0.02}_{-0.02}{}^{+0.06}_{-0.06}$
$N_t \ge 2,\ N_b \ge 2,\ 200 \le M_{T2} < 300$ GeV							
200 – 275	6	$16^{+3}_{-3}{}^{+2}_{-2}$	$8^{+3}_{-2}{}^{+2}_{-2}$	$8^{+1}_{-1}{}^{+1}_{-1}$	$0.14^{+0.01}_{-0.01}{}^{+0.11}_{-0.11}$	$0.7^{+0.5}_{-0.5}{}^{+0.6}_{-0.6}$	$0.33^{+0.03}_{-0.03}{}^{+0.11}_{-0.11}$
275 – 350	1	$3.3^{+1.3}_{-1.1}{}^{+0.5}_{-0.5}$	$1.6^{+1.0}_{-0.8}{}^{+0.4}_{-0.4}$	$1.6^{+0.8}_{-0.6}{}^{+0.3}_{-0.3}$	$0.05^{+0.01}_{-0.01}{}^{+0.04}_{-0.04}$	$0.00^{+0.23}_{-0.23}{}^{+0.17}_{-0.00}$	$0.06^{+0.01}_{-0.01}{}^{+0.02}_{-0.02}$
350+	0	$1.3^{+0.9}_{-0.4}{}^{+0.1}_{-0.1}$	$0.18^{+0.58}_{-0.18}{}^{+0.04}_{-0.04}$	$1.0^{+0.7}_{-0.4}{}^{+0.1}_{-0.1}$	$0.02^{+0.00}_{-0.00}{}^{+0.02}_{-0.02}$	$0.00^{+0.09}_{-0.09}{}^{+0.06}_{-0.00}$	$0.04^{+0.01}_{-0.01}{}^{+0.01}_{-0.01}$
$N_t \ge 2,\ N_b \ge 2,\ 300 \le M_{T2} < 400$ GeV							
200 – 275	10	$7.1^{+1.8}_{-1.5}{}^{+0.8}_{-0.7}$	$3.5^{+1.4}_{-1.1}{}^{+0.6}_{-0.6}$	$3.2^{+1.1}_{-1.0}{}^{+0.3}_{-0.3}$	$0.12^{+0.01}_{-0.01}{}^{+0.10}_{-0.10}$	$0.06^{+0.04}_{-0.04}{}^{+0.46}_{-0.06}$	$0.18^{+0.02}_{-0.02}{}^{+0.06}_{-0.06}$
275 – 350	2	$1.7^{+1.3}_{-0.7}{}^{+0.2}_{-0.2}$	$0.6^{+1.1}_{-0.6}{}^{+0.1}_{-0.1}$	$0.83^{+0.63}_{-0.31}{}^{+0.10}_{-0.10}$	$0.09^{+0.01}_{-0.01}{}^{+0.08}_{-0.08}$	$0.00^{+0.02}_{-0.02}{}^{+0.02}_{-0.00}$	$0.13^{+0.02}_{-0.02}{}^{+0.04}_{-0.04}$
350+	1	$0.8^{+1.0}_{-0.3}{}^{+0.2}_{-0.2}$	$0.00^{+0.77}_{-0.00}{}^{+0.00}_{-0.00}$	$0.6^{+0.6}_{-0.3}{}^{+0.2}_{-0.2}$	$0.05^{+0.01}_{-0.01}{}^{+0.04}_{-0.04}$	$0.01^{+0.04}_{-0.04}{}^{+0.04}_{-0.01}$	$0.07^{+0.01}_{-0.01}{}^{+0.02}_{-0.02}$
$N_t \ge 2,\ N_b \ge 2,\ M_{T2} > 400$ GeV							
200 – 350	1	$0.27^{+1.00}_{-0.16}{}^{+0.05}_{-0.05}$	$0.00^{+0.82}_{-0.00}{}^{+0.00}_{-0.00}$	$0.21^{+0.57}_{-0.16}{}^{+0.03}_{-0.03}$	$0.03^{+0.00}_{-0.00}{}^{+0.03}_{-0.03}$	$0.00^{+0.02}_{-0.00}{}^{+0.01}_{-0.00}$	$0.03^{+0.01}_{-0.01}{}^{+0.01}_{-0.01}$
350+	1	$0.41^{+1.27}_{-0.06}{}^{+0.19}_{-0.17}$	$0.00^{+1.14}_{-0.00}{}^{+0.00}_{-0.00}$	$0.05^{+0.55}_{-0.04}{}^{+0.01}_{-0.01}$	$0.16^{+0.01}_{-0.01}{}^{+0.17}_{-0.16}$	$0.00^{+0.04}_{-0.04}{}^{+0.02}_{-0.00}$	$0.19^{+0.02}_{-0.02}{}^{+0.07}_{-0.07}$

and mistagging (up to 5%). The HPTT analysis also considers uncertainties from the pileup description (up to 30%). All these uncertainties, apart from those arising from the simulation sample size, are treated as fully correlated between search bins when computing exclusion limits.

For the HPTT analysis, all 50 search region bins, as well as the 21 single-lepton control region bins, are fit simultaneously in order to evaluate the cross section excluded at 95% confidence level for each benchmark signal point. The inclusion of the single-lepton control regions in the simultaneous fit ensures that any potential signal contamination in these regions, based on the corresponding estimated event yields for any given signal model, is taken into account in the signal strength excluded by the maximum likelihood fit. The systematic uncertainties assigned to the signal and background predictions are treated as nuisance parameters in the fit.

Signal contamination is treated in a different, but equivalent, way for the HETT results. The expected contribution of a potential signal to the single-lepton control regions is translated to an expectation for the search regions in the same way as done for the backgrounds. The yields per search region obtained in this way are then subtracted from the nominal signal yield predictions. As such, the effect of signal contamination in the control regions is to reduce the signal efficiency.

Figures 15 and 16 show the 95% CL exclusion limits obtained by the HPTT and HETT analyses, respectively, for simplified models in the pure T2tt scenario, and in the mixed T2tb scenario assuming a 50% branching fraction for each of the two decay modes ($\tilde{t} \to t\tilde{\chi}_1^0 / \tilde{t} \to b\tilde{\chi}_1^{\pm}$). In the latter case, the $\tilde{\chi}_1^{\pm}$ and $\tilde{\chi}_1^0$ are assumed to be nearly degenerate in mass, with a 5 GeV difference between their masses. The limits obtained by the two analyses are comparable. Using the 2.3 fb^{-1}dataset, stop masses up to 780 GeV and LSP masses up to 260 GeV are probed in the T2tt scenario. In the T2tb scenario, stop masses up to 750 GeV and LSP masses up to 280 GeV are probed.

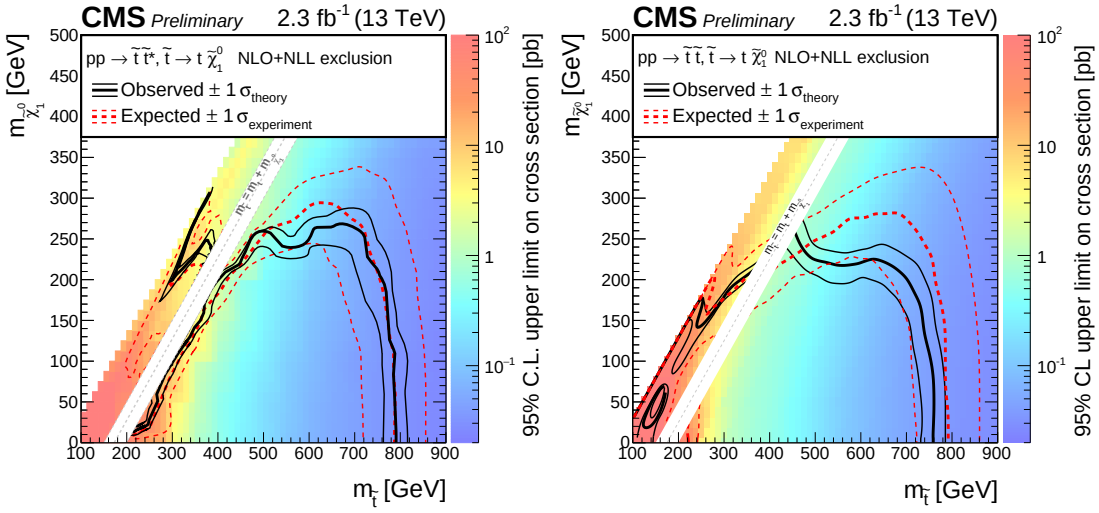

Figure 15: HPTT (left) and HETT (right) exclusion limits at 95% CL for simplified models of top squark pair production in the T2tt scenario. The solid black curves represent the observed exclusion contours with respect to NLO+NLL cross section calculations [55] and the corresponding ± 1 standard deviations. The dashed red curves indicate the expected exclusion contour and the ± 1 standard deviations with experimental uncertainties. The white diagonal band corresponds to $|m_{\tilde{t}} - m_t| < 25\,\text{GeV}$.

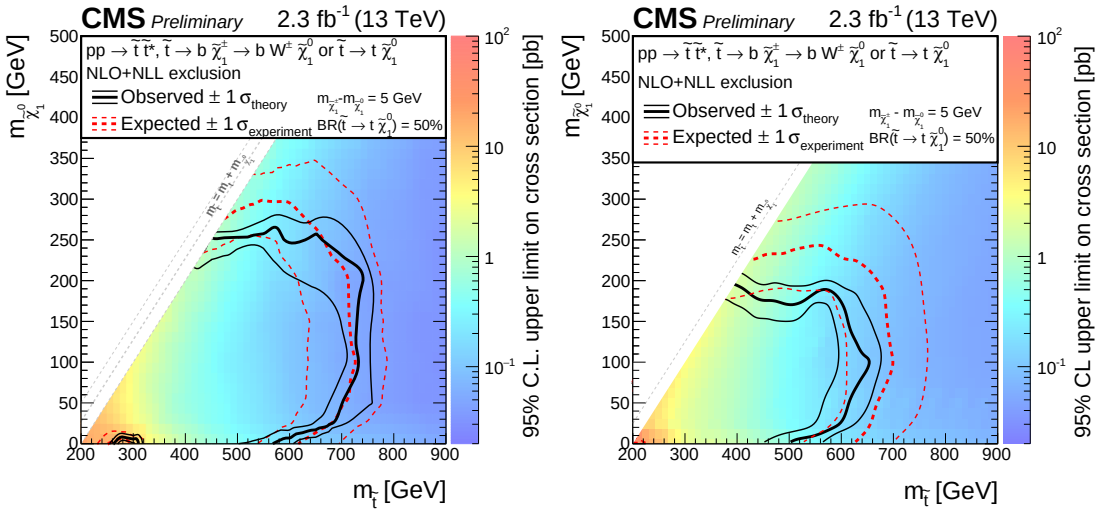

Figure 16: HPTT (left) and HETT (right) exclusion limits at 95% CL for simplified models of top squark pair production in the T2tb scenario, assuming a 50% branching ratio for each of the $\tilde{t} \to t\tilde{\chi}_1^0/\tilde{t} \to b\tilde{\chi}_1^{\pm}$ modes and a 5 GeV mass difference between the $\tilde{\chi}_1^{\pm}$ and $\tilde{\chi}_1^0$ (right). The solid black curves represent the observed exclusion contours with respect to NLO+NLL cross section calculations [55] and the corresponding ± 1 standard deviations. The dashed red curves indicate the expected exclusion contour and the ± 1 standard deviations with experimental uncertainties.

6 Summary

The results of a search for direct top squark pair production in the all-hadronic final state have been presented. The search uses events with jets and large $\not{E}_T$, selected from a data sample corresponding to an integrated luminosity of 2.3 fb^{-1} collected in proton-proton collisions at a center-of-mass energy of 13 TeV with the CMS detector. Two complementary analyses that are optimized to provide sensitivity for a variety of different signal topologies are performed. No statistically significant excess of events above the expected standard model background is observed, and exclusion limits are set at the 95% confidence level in the context of simplified models of direct top squark pair production. For simplified models in which both top squarks decay to a top quark and a neutralino, top squark masses up to 780 GeV and neutralino masses up to 260 GeV are probed. In the case of models that assume 50% branching fractions for top squark decays to a top quark and a neutralino, or to a bottom quark and a chargino that is nearly degenerate in mass with respect to the neutralino, top squark masses up to 750 GeV and neutralino masses up to 280 GeV are probed.

References

[1] R. Barbieri, S. Ferrara, and C. A. Savoy, "Gauge Models with Spontaneously Broken Local Supersymmetry", *Phys. Lett.* **B119** (1982) 343, doi:10.1016/0370-2693(82)90685-2.

[2] S. Dawson, E. Eichten, and C. Quigg, "Search for Supersymmetric Particles in Hadron - Hadron Collisions", *Phys. Rev.* **D31** (1985) 1581, doi:10.1103/PhysRevD.31.1581.

[3] H. P. Nilles, "Supersymmetry, Supergravity and Particle Physics", *Phys. Rept.* **110** (1984) 1, doi:10.1016/0370-1573(84)90008-5.

[4] H. E. Haber and G. L. Kane, "The Search for Supersymmetry: Probing Physics Beyond the Standard Model", *Phys. Rept.* **117** (1985) 75, doi:10.1016/0370-1573(85)90051-1.

[5] D. Chung et al., "The soft supersymmetry breaking Lagrangian: Theory and applications", *Phys. Rept.* **407** (2005) 1, doi:10.1016/j.physrep.2004.08.032, arXiv:hep-ph/0312378.

[6] J. Wess and B. Zumino, "Supergauge Transformations in Four-Dimensions", *Nucl. Phys.* **B70** (1974) 39, doi:10.1016/0550-3213(74)90355-1.

[7] G. R. Farrar and P. Fayet, "Phenomenology of the Production, Decay, and Detection of New Hadronic States Associated with Supersymmetry", *Phys. Lett.* **B76** (1978) 575, doi:10.1016/0370-2693(78)90858-4.

[8] J. L. Feng, "Dark Matter Candidates from Particle Physics and Methods of Detection", *Annual Review of Astronomy and Astrophysics* **48** (2010) 495, doi:10.1146/annurev-astro-082708-101659, arXiv:1003.0904.

[9] G. 't Hooft, "Naturalness, chiral symmetry, and spontaneous chiral symmetry breaking", *NATO Sci. Ser.* **B59** (1980) 135.

[10] E. Witten, "Dynamical Breaking of Supersymmetry", *Nucl. Phys.* **B188** (1981) 513, doi:10.1016/0550-3213(81)90006-7.

[11] M. Dine, W. Fischler, and M. Srednicki, "Supersymmetric Technicolor", *Nucl. Phys.* **B189** (1981) 575, doi:10.1016/0550-3213(81)90582-4.

[12] S. Dimopoulos and S. Raby, "Supercolor", *Nucl. Phys.* **B192** (1981) 353, doi:10.1016/0550-3213(81)90430-2.

[13] S. Dimopoulos and H. Georgi, "Softly Broken Supersymmetry and SU(5)", *Nucl. Phys.* **B193** (1981) 150, doi:10.1016/0550-3213(81)90522-8.

[14] R. K. Kaul and P. Majumdar, "Cancellation of Quadratically Divergent Mass Corrections in Globally Supersymmetric Spontaneously Broken Gauge Theories", *Nucl. Phys.* **B199** (1982) 36, doi:10.1016/0550-3213(82)90565-X.

[15] N. Sakai, "Naturalness in Supersymmetric Guts", *Z. Phys.* **C11** (1981) 153, doi:10.1007/BF01573998.

[16] M. Papucci, J. T. Ruderman, and A. Weiler, "Natural SUSY Endures", *JHEP* **09** (2012) 035, doi:10.1007/JHEP09(2012)035, arXiv:1110.6926.

[17] C. Brust, A. Katz, S. Lawrence, and R. Sundrum, "SUSY, the Third Generation and the LHC", *JHEP* **03** (2012) 103, doi:10.1007/JHEP03(2012)103, arXiv:1110.6670.

[18] A. Delgado et al., "The light stop window", *Eur. Phys. J.* **C73** (2013) 2370, doi:10.1140/epjc/s10052-013-2370-5, arXiv:1212.6847.

[19] J. L. Feng, "Naturalness and the Status of Supersymmetry", *Ann. Rev. Nucl. Part. Sci.* **63** (2013) 351, doi:10.1146/annurev-nucl-102010-130447, arXiv:1302.6587.

[20] L. Evans and P. Bryant (editors), "LHC Machine", *JINST* **3** (2008) S08001, doi:10.1088/1748-0221/3/08/S08001.

[21] ATLAS Collaboration, "ATLAS Run 1 searches for direct pair production of third-generation squarks at the Large Hadron Collider", *Eur. Phys. J.* **C75** (2015), no. 10, 510, doi:10.1140/epjc/s10052-015-3726-9, arXiv:1506.08616.

[22] CMS Collaboration, "Search for direct pair production of supersymmetric top quarks decaying to all-hadronic final states in pp collisions at sqrt(s) = 8 TeV", arXiv:1603.00765. Submitted to Eur. Phys. J. C.

[23] CMS Collaboration, "Exclusion limits on gluino and top-squark pair production in natural SUSY scenarios with inclusive razor and exclusive single-lepton searches at 8 TeV.", Technical Report CMS-PAS-SUS-14-011, CERN, Geneva, 2014.

[24] CMS Collaboration, "Search for top-squark pair production in the single-lepton final state in pp collisions at $\sqrt{s}$ = 8 TeV", *Eur. Phys. J.* **C73** (2013), no. 12, 2677, doi:10.1140/epjc/s10052-013-2677-2, arXiv:1308.1586.

[25] CMS Collaboration, "Search for supersymmetry in events with soft leptons, low jet multiplicity, and missing transverse momentum in proton-proton collisions at sqrt(s) = 8 TeV", Technical Report CMS-PAS-SUS-14-021, CERN, Geneva, 2015.

[26] CMS Collaboration, "Search for supersymmetry in pp collisions at $\sqrt{s}$=8 TeV in events with a single lepton, large jet multiplicity, and multiple b jets", *Phys. Lett.* **B733** (2014) 328–353, doi:10.1016/j.physletb.2014.04.023, arXiv:1311.4937.

[27] J. Alwall, P. Schuster, and N. Toro, "Simplified Models for a First Characterization of New Physics at the LHC", *Phys. Rev.* **D79** (2009) 075020, doi:10.1103/PhysRevD.79.075020, arXiv:0810.3921.

[28] J. Alwall, M.-P. Le, M. Lisanti, and J. G. Wacker, "Model-Independent Jets plus Missing Energy Searches", *Phys. Rev.* **D79** (2009) 015005, doi:10.1103/PhysRevD.79.015005, arXiv:0809.3264.

[29] LHC New Physics Working Group Collaboration, "Simplified Models for LHC New Physics Searches", *J. Phys.* **G39** (2012) 105005, doi:10.1088/0954-3899/39/10/105005, arXiv:1105.2838.

[30] C. Lester and D. Summers, "Measuring masses of semiinvisibly decaying particles pair produced at hadron colliders", *Phys.Lett.* **B463** (1999) 99–103, doi:10.1016/S0370-2693(99)00945-4, arXiv:hep-ph/9906349.

[31] A. Barr, C. Lester, and P. Stephens, "m(T2): The Truth behind the glamour", *J.Phys.* **G29** (2003) 2343–2363, doi:10.1088/0954-3899/29/10/304, arXiv:hep-ph/0304226.

[32] CMS Collaboration, "Particle-Flow Event Reconstruction in CMS and Performance for Jets, Taus, and $\not\!\!E_{\mathrm{T}}$", CMS Physics Analysis Summary CMS-PAS-PFT-09-001, 2009.

[33] CMS Collaboration, "Commissioning of the Particle-flow Event Reconstruction with the first LHC collisions recorded in the CMS detector", CMS Physics Analysis Summary CMS-PAS-PFT-10-001, 2010.

[34] M. Cacciari, G. P. Salam, and G. Soyez, "The anti-k_t jet clustering algorithm", *JHEP* **04** (2008) 063, doi:10.1088/1126-6708/2008/04/063, arXiv:0802.1189.

[35] CMS Collaboration, "Identification of b-quark jets with the CMS experiment", *JINST* **8** (2013) P04013, doi:10.1088/1748-0221/8/04/P04013, arXiv:1211.4462.

[36] CMS Collaboration, "Performance of b tagging at $\sqrt{s} = 8$ TeV in multijet, $\mathrm{t\bar{t}}$ and boosted topology events", CMS Physics Analysis Summary CMS-PAS-BTV-13-001, CERN, 2013.

[37] CMS Collaboration, "Boosted Top Jet Tagging at CMS", CMS Physics Analysis Summary CMS-PAS-JME-13-007, CERN, 2014.

[38] CMS Collaboration, "Top Tagging with New Approaches", CMS Physics Analysis Summary CMS-PAS-JME-15-002, CERN, 2016.

[39] CMS Collaboration, "Searches for third-generation squark production in fully hadronic final states in proton-proton collisions at $\sqrt{s} = 8$ TeV", *JHEP* **06** (2015) 116, doi:10.1007/JHEP06(2015)116, arXiv:1503.08037.

[40] D. E. Kaplan, K. Rehermann, M. D. Schwartz, and B. Tweedie, "Top Tagging: A Method for Identifying Boosted Hadronically Decaying Top Quarks", *Phys. Rev. Lett.* **101** (2008) 142001, doi:10.1103/PhysRevLett.101.142001, arXiv:0806.0848.

[41] T. Plehn, M. Spannowsky, M. Takeuchi, and D. Zerwas, "Stop Reconstruction with Tagged Tops", *JHEP* **1010** (2010) 078, doi:10.1007/JHEP10(2010)078, arXiv:1006.2833.

[42] D. E. Kaplan, K. Rehermann, and D. Stolarski, "Searching for Direct Stop Production in Hadronic Top Data at the LHC", *JHEP* **1207** (2012) 119, doi:10.1007/JHEP07(2012)119, arXiv:1205.5816.

[43] CMS Collaboration, "Performance of electron reconstruction and selection with the CMS detector in proton-proton collisions at $\sqrt{s} = 8$ TeV", *JINST* **10** (2015) P06005, doi:10.1088/1748-0221/10/06/P06005, arXiv:1502.02701.

[44] CMS Collaboration, "Performance of CMS muon reconstruction in pp collision events at $\sqrt{s} = 7$ TeV", *JINST* **7** (2012) P10002, doi:10.1088/1748-0221/7/10/P10002, arXiv:1206.4071.

[45] J. Alwall et al., "MadGraph5: going beyond", *JHEP* **06** (2011) 128, doi:10.1007/JHEP06(2011)128, arXiv:1106.0522.

[46] NNPDF Collaboration, "Parton distributions for the LHC Run II", *JHEP* **04** (2015) 040, doi:10.1007/JHEP04(2015)040, arXiv:1410.8849.

[47] P. Nason, "A New method for combining NLO QCD with shower Monte Carlo algorithms", *JHEP* **11** (2004) 040, doi:10.1088/1126-6708/2004/11/040, arXiv:hep-ph/0409146.

[48] S. Frixione, P. Nason, and C. Oleari, "Matching NLO QCD computations with Parton Shower simulations: the POWHEG method", *JHEP* **11** (2007) 070, doi:10.1088/1126-6708/2007/11/070, arXiv:0709.2092.

[49] S. Alioli, P. Nason, C. Oleari, and E. Re, "A general framework for implementing NLO calculations in shower Monte Carlo programs: the POWHEG BOX", *JHEP* **06** (2010) 043, doi:10.1007/JHEP06(2010)043, arXiv:1002.2581.

[50] E. Re, "Single-top Wt-channel production matched with parton showers using the POWHEG method", *Eur. Phys. J.* **C71** (2011) 1547, doi:10.1140/epjc/s10052-011-1547-z, arXiv:1009.2450.

[51] J. Alwall et al., "The automated computation of tree-level and next-to-leading order differential cross sections, and their matching to parton shower simulations", *JHEP* **07** (2014) 079, doi:10.1007/JHEP07(2014)079, arXiv:1405.0301.

[52] T. Sjostrand, S. Mrenna, and P. Z. Skands, "A Brief Introduction to PYTHIA 8.1", *Comput. Phys. Commun.* **178** (2008) 852–867, doi:10.1016/j.cpc.2008.01.036, arXiv:0710.3820.

[53] GEANT4 Collaboration, "GEANT4—a simulation toolkit", *Nucl. Instrum. Meth. A* **506** (2003) 250, doi:10.1016/S0168-9002(03)01368-8.

[54] S. Abdullin et al., "The fast simulation of the CMS detector at LHC", *J. Phys. Conf. Ser.* **331** (2011) 032049, doi:10.1088/1742-6596/331/3/032049.

[55] C. Borschensky et al., "Squark and gluino production cross sections in pp collisions at $\sqrt{s}$ = 13, 14, 33 and 100 TeV", *Eur. Phys. J.* **C74** (2014), no. 12, 3174, doi:10.1140/epjc/s10052-014-3174-y, arXiv:1407.5066.

[56] CMS Collaboration, "Identification of b quark jets at the CMS Experiment in the LHC Run 2", Technical Report CMS-PAS-BTV-15-001, CERN, 2016.

[57] CMS Collaboration, "Search for new physics with the MT2 variable in all-jets final states produced in pp collisions at sqrt(s) = 13 TeV", arXiv:1603.04053. Submitted to JHEP.

[58] B. Efron, "The Jackknife, The Bootstrap and Other Resampling Plans", volume 38 of *CBMS-NSF Regional Conference Series in Applied Mathematics*. SIAM, Philadelphia, 1982.

[59] CMS Collaboration, "Observation of top quark pairs produced in association with a vector boson in pp collisions at $\sqrt{s} = 8$ TeV", *JHEP* **01** (2016) 096, doi:10.1007/JHEP01(2016)096, arXiv:1510.01131.

[60] S. Catani, D. de Florian, M. Grazzini, and P. Nason, "Soft gluon resummation for Higgs boson production at hadron colliders", *JHEP* **07** (2003) 028, doi:10.1088/1126-6708/2003/07/028, arXiv:hep-ph/0306211.

[61] M. Cacciari et al., "The $t\bar{t}$ cross-section at 1.8 TeV and 1.96 TeV: a study of the systematics due to parton densities and scale dependence", *JHEP* **04** (2004) 068, doi:10.1088/1126-6708/2004/04/068, arXiv:hep-ph/0303085.

[62] Particle Data Group, K. A. Olive et al., "Review of Particle Physics", *Chin. Phys. C* **38** (2014) 090001, doi:10.1088/1674-1137/38/9/090001.

[63] ATLAS and CMS Collaborations, "Procedure for the LHC Higgs boson search combination in summer 2011", Technical Report ATL-PHYS-PUB-2011-011, CMS NOTE-2011/005, CERN, Geneva, Aug, 2011.